Metallurgical and Materials Transactions B, Vol. 27B, No. 4 (August), 1996, pp. 672-685.

FLOW AND THERMAL BEHAVIOR OF THE TOP SURFACE FLUX/POWDER LAYERS IN CONTINUOUS CASTING MOLDS

R. M. McDavid and B. G. Thomas
Department of Mechanical and Industrial Engineering
University of Illinois at Urbana-Champaign
1206 W. Green Street
Urbana, IL 61801

ABSTRACT

Steady-state finite-element models have been formulated to investigate the coupled fluid flow and thermal behavior of the top-surface flux layers in continuous casting of steel slabs. The 3-D FIDAP™ model includes the shear stresses imposed on the flux/steel interface by flow velocities calculated in the molten steel pool. It also includes different temperature-dependent powder properties for solidification and melting. Good agreement between the 3-D model and experimental measurements was obtained. The shear forces, imposed by the steel surface motion towards the SEN, create a large recirculation zone in the liquid flux pool. Its depth increases with increasing casting speed, increasing liquid flux conductivity and decreasing flux viscosity. For typical conditions, this zone contains almost 4 kg of flux, which contributes to an average residence time of about 2 minutes. Additionally, because the shear forces produced by the narrowface consumption and the steel flow oppose each other, the flow in the liquid flux layer separates at a location centered 200 mm from the narrowface wall. This flow separation depletes the liquid flux pool at this location and may contribute to generically poor feeding of the mold-strand gap there. As a further consequence, a relatively cold spot develops at the wideface mold wall near the separation point. This non-uniformity in the temperature distribution may result in non-uniform heat removal, and possibly non-uniform initial shell growth in the meniscus region along the wideface off-corner region. In this way, potential steel quality problems may be linked to flow in the liquid flux pool.

I. INTRODUCTION

In the continuous casting process, mold flux is added as a powder on to the surface of the liquid steel. The flux absorbs heat from the molten steel, sinters and melts into a pool of liquid, beneath the floating powder. Below the liquid flux layer, steel enters the mold cavity through the submerged entry nozzle (SEN), recirculates up the narrowface wall and along the top-surface, and flows back towards the SEN (see Figure 1). The top surface flux layers provide thermal and chemical insulation of the top surface of the liquid steel and aid in the removal of non-metallic inclusions. The liquid flux then infiltrates the gap between the mold wall and the solidifying steel strand, where it acts as a lubricant and promotes slow, uniform heat transfer in the mold-strand gap. Collectively, these functions work to reduce such problems as surface and sub-surface inclusions, non-uniform shell growth and breakouts, surface depressions and cracks.

Given the impact that the mold flux has on steel slab quality, many previous studies have investigated various aspects of powder/flux behavior. Most have been experimental or industrial. For example, studies performed at Nippon Steel[1, 2] and Inland Steel[3] have confirmed an inverse-relationship between optimum liquid flux viscosity and casting speed to achieve uniform heat flow and effective lubrication in the mold-stand gap. Other work by Sardemann and Schrewe[4] has shown the importance of maintaining a sufficiently-thick liquid slag layer. Specifically, they found that the formation of cracks in the steel slab is reduced by a thick liquid flux layer. Sufficiently-thick liquid slag layers are also important to prevent carbon "pick-up" by the steel from the flux, as reported by Nakato and co-workers[5].

Several researchers have characterized the formation of the liquid flux layer using the empirical property of "melting rate"[6-8]. For example, Branion[7] comments that the melting rate determines the ability of the flux to maintain a stable liquid layer. Using apparatus developed by Lindefelt and Hasselstrom[9], several investigators have measured the rate at which molten flux is produced. This melting rate decreases with increasing carbon present in the flux, as demonstrated by Xie[6].

Flux behavior has also been investigated using mathematical models. Most previous models attempt to characterize flux behavior in the thin mold-strand gap[10-17]. Bommaraju et al.[10] modeled flux flow as Couette flow between the stationary copper mold and the steel shell moving at the casting speed. Anzai and co-workers[14] go a step further by solving the 1-D Navier-Stokes equation which includes the pressure term neglected in the work by Bommaraju. Anzai predicted that the flow-rate of flux increases as viscosity is decreased, and that the trend in flow-rate and fluid pressure follow the same temporal pattern as the mold-oscillation speed. Several heat transfer models of the gap have been developed, where an effective thermal resistance of the gap layers is sought[15-17].

Only a few models have analyzed the important top-surface flux layers[13, 18, 19]. Most of these are one-dimensional heat-conduction analyses. The study by Nakato and co-workers[13] solved the one-dimensional heat conduction equation to find that the liquid layer thickness increases with the square-root of time. The growth constant in the equation was related to the melting point and thermal conductivity of the flux, and to process parameters such as the steel surface temperature. Dehalle et

al.[18] showed, using a similar model, that there is no significant change in liquid layer thickness with further additions of powder when the surface temperature is kept below 800°C.

A more detailed model of the top-surface flux layer was developed by Nakano and co-workers[19]. In their model, the flux domain was discretized into a series of thin horizontal layers, and the one-dimensional heat conduction equation was solved over each layer. This model accurately accounted for the difference in material properties of the various forms of the flux as it transforms from powder to liquid. For steady state conditions, the model results agreed well with experiment. However, the liquid thermal conductivity in the model had to be arbitrarily increased to 4 times the powder value to obtain this agreement. An increase of 6 times was need to match the experiment when flux consumption was incorporated. Their conclusion was that convection in the liquid pool is a significant heat transfer mechanism, particularly when consumption is present.

Based on this brief review, there remain several opportunities for improved mathematical models to help understand behavior of the flux. Relatively few models focus on behavior of the top-surface flux layers, although experimental work has demonstrated the importance of the thickness of the top-surface liquid flux available to supply the gap. All of the heat transfer models reviewed consider only conduction of heat, despite confirmation of the importance of radiation through the liquid flux[16, 19-21] and the significance of convection in the liquid flux pool to heat transfer[19, 22]. Furthermore, none of the models reviewed consider the effects of either steel motion or flow in the top surface liquid flux pool.

The present work applies a three-dimensional (3-D) coupled heat-transfer and fluid-flow finite-element model to analyze the behavior of the top surface flux layers. It aims to more accurately quantify the phenomena of powder melting and liquid flux behavior in an operating caster. The commercial finite element package FIDAP is used to solve the model equations. A 3-D formulation was needed because preliminary 1-D and 2-D models did not produce quantitative results (they necessarily neglect the important phenomena of convection and 3-D mass consumption flow). The results of the 3-D model are verified experimentally, using data collected at the operating caster at LTV Steel in Cleveland[17, 23]. An initial parametric study is performed to ascertain the effect of process parameters such as viscosity and thermal conductivity. Finally, a 1-D transient model is developed to explore the validity of the steady-state assumption.

II. MODEL FORMULATION

A. *Model Assumptions*

3-D coupled fluid flow and heat transfer with change of phase in the powder, liquid and re-solidified flux layers was modeled in this study. The model accounts for the known location and shape of the steel/flux interface, momentum transfer between the liquid steel and flux and radiative and natural convective heat loss at the free surface of the flux. A separate 3-D model is used to calculate the flow field in the liquid steel[24]. This steel flow model and the flux flow model presented here are coupled through the shear stress distribution at their mutual interface. Separate temperature-dependent

functions for powder viscosity and thermal conductivity are applied in regions of melting and solidifying powder.

Model assumptions include:

(i) Flow is laminar. This is consistent with Re ≈ 70 (see Table I)

(ii) The flow and thermal fields are both steady. This assumption is investigated in section VII with the 1-D transient model.

(iii) Steel surface shape is fixed according to measurements made under steady operating conditions. Thus, surface waves and sloshing are ignored.

(iv) Flux properties are characterized solely through the macroscopic material properties of viscosity, thermal conductivity, specific heat, latent heat and density. Effects of microscopic kinetic effects such as particle sintering are manifested only in the values of these macroscopic properties.

(v) Density is constant and gravity is ignored. The model neglects buoyancy effects due to the known density increase as the powder sinters and melts. The estimated Raleigh Number is ~ 10^5 - 10^6, which is high enough that natural convection should be important, but low enough that the flow does not become turbulent. The modified Froude Number[25] of only 0.077 (Table I) shows that even relative to the driving force of the steel motion, natural convection is important. Thus, there is a significant tendency for the powder to float above the liquid flux layer while gravity induces flow of the liquid flux downwards into the valleys in the steel surface contours.

(vi) Powder feeding is uniform and steady over the entire mold area. In practice this assumption is only approximated by very careful operators or automatic powder feeders.

(vii) Mold oscillation has no role other than to impose the constant, uniform, consumption rate of liquid flux into the mold - strand gap around the perimeter of the mold.

(viii) Powder and liquid flux both behave as an isotropic Newtonian fluid with temperature-dependent viscosity, thermal conductivity, and enthalpy.

(ix) Thermal contact resistance between the molten steel and molten flux layers is negligible.

(x) Viscous dissipation energy is negligible because the Brinkman Number is only 10^{-9} (see Table I).

B. *Governing Equations*

Based on the problem and assumptions posed in the preceding section, the following 5 continuum equations are solved.

$$\nabla \cdot \mathbf{u} = 0 \qquad [1]$$

$$\rho\, \mathbf{u} \cdot \nabla \mathbf{u} = -\nabla P + \mu(T)\, \nabla \cdot \nabla \mathbf{u} \qquad [2]$$

$$\rho C_p \left[\mathbf{u} \cdot \nabla T\right] = \nabla \cdot \left(k(T)\, \nabla T\right) \qquad [3]$$

They represent mass, momentum and energy conservation in three dimensions respectively. Nomenclature is defined in Table I.

C. *Geometry Definition and Boundary Conditions*

Schematics of the model domain with dimensions are given in Figures 2 and 3. Computational requirements are reduced by invoking bi-fold symmetry to model only one quarter of the physical domain. The exact shape of the steel-flux interface used was imposed based on steady measurements on an actual caster[17, 23], as described later. The shape of the meniscus portion of this interface is determined from an analytical solution of a modified version of the Young-Laplace Equation.[26, 27]

The flow boundary conditions are given in Figure 4, with the finite element mesh. At the flux/steel interface, a fixed shear stress, τ_{zx}, condition was imposed.

$$\tau_{zx} = \mu \frac{\partial u_x}{\partial n}\bigg|_{flux} = \mu_{steel} \frac{\partial u_x}{\partial n}\bigg|_{steel} \qquad [4]$$

The value of τ_{zx} was calculated by iterating between the present 3-D isothermal flow model of flux flow and a 3-D model of turbulent flow in the liquid steel[24], with the typical flow pattern shown in Figure 5. Shear stress from the top surface of the steel model is applied to the bottom surface of the flux model. Interface velocities from the flux model are then applied to the steel flow model. Iteration continues until both stress and velocity at the flux-steel interface agree. The shear stress solution along the flux / steel interface increases from zero at the narrowface and SEN to a maximum of about 0.26 Nm^{-2} near the center.

A uniform consumption rate of liquid flux around the mold perimeter is imposed by fixing the z-velocities into the top free surface and the y-velocities out of the bottom layer of elements along the wideface. (Appendix A.) The meniscus region and mold-strand gap are not modeled along the wideface, where the domain is offset from the wall. Studies using 2-D domains parallel to the narrowface revealed this simplification does not significantly affect the flow.[23]

Thermal boundary conditions are given in Figure 6. The effective heat transfer coefficient from the top surface h_{eff} (Equation B3) is dominated by radiation but also includes natural convection in air.

III *Material Property Data*

A. *Viscosity-Temperature Relationship*

The three forms of flux, (powder, liquid and glassy/crystalline solid), were simulated using two different material models, in different parts of the domain. One part characterizes the flux as liquid cooling to a coherent solid near the mold walls (solidifying). The other part models the powder as it sinters and melts to form the liquid in all other regions of the mold (melting). The viscosity of the powder was estimated from rheological data used in the field of particle fluidization[30-36], assuming a mean particle size of 250 μm and an average density of 1000 kgm^{-3}. The liquid viscosity follows the well-documented exponential function of temperature[3, 10, 28, 29]. The maximum viscosity of resolidified flux was truncated at 10^4 Pa.s to avoid numerical instability. Figure 7 shows the data

chosen to approximate the viscosity-temperature relationships of fluxes with two typical viscosities — standard (Case 1) and high viscosity (Case 2).

B. ***Thermal Conductivity-Temperature Relationship***

The thermal conductivity of the flux was also modeled differently for melting and solidification. The pair of curves are given in Figure 8. The thermal conductivity of sintering powder gradually increases as air spaces disappear. For both melting and solidifying flux, the standard effective thermal conductivity above the melting temperature, k_f, was fixed at 3 $Wm^{-1}K^{-1}$. This typical value[19, 22, 37], assumes no convection but includes both conduction and radiation through the transparent liquid. Below the sintering temperature (900°C), the conductivities reported by Taylor and Mills[21] are used for the melting powder, assumed over most of the domain. In the totally solid state, a constant value of 0.9 $Wm^{-1}K^{-1}$ was adopted, according to Taylor and Mills[21] and Nagata et al.[38].

C. ***Enthalpy-Temperature Relationship***

An enthalpy-temperature model is used to simulate solidification/melting of the flux. This is believed to be more stable and accurate than an "enhanced specific heat" model. The assumed function, shown in Figure 9, is based on sparse data from available literature.[37, 40] It includes a latent heat of fusion of 350 $kJkg^{-1}$ at the melting point of 1000°C.

IV. SOLUTION METHODOLOGY

The preceding governing equations, subject to the boundary conditions discussed, were solved using the finite element method with the commercial CFD code FIDAP. Full details of the implementation of this model are found in the FIDAP Theoretical Manual[41] and elsewhere[23].

The Navier-Stokes and continuity equations were solved using a mixed (i.e. **u**-P) formulation. Successive Substitution proved to be more robust than the Newton-Raphson Method for solving the non-linear algebraic finite element equations. Oscillatory behavior was suppressed with an under-relaxation coefficient between 0.3 and 0.4 (FIDAP acceleration factor between 0.7 and 0.6), meaning that the guess used to linearize the equations relied more heavily on the past solution than on the most recent solution. A solution was considered converged when the normalized residual L-2 norm (RCONV in FIDAP) fell below the user-specified value of 0.01. Additionally, a smooth monotonically-decreasing residual norm was generally indicative that a good solution was being achieved.

The inherent high non-linearity in the momentum equations and the two-way coupling with the energy equation, together make this problem difficult to converge. Thus, a good initial guess of the flow field and temperature distribution was required to avoid divergence. The solution strategy developed to consistently and efficiently obtain a converged solution is illustrated in Figure 10. The first step solves an isothermal flow problem, assuming a constant density of 2500 kgm^{-3} and constant viscosity of 0.03 Pa.s, which is the correct value at the flux / steel interface.

The final mesh, shown in Figures 4 and 6 consisted of 3640 27-noded (i.e. quadratic) brick elements and a total of 28500 nodes. Calculations were performed on a CRAY Y-MP supercomputer

using a "direct iterative solver" in FIDAP. The computational requirements are summarized in Table II. Initial attempts using the "indirect (segregated) solver" in FIDAP were unsuccessful, as the 15-fold savings in cost per iteration was more than offset by a 30-fold increase in number of iterations required for convergence. All pre- and post-processing was performed on a Silicon Graphics Personal Iris 4D/25 with 64 MB of RAM, and over 400 MB of disk space.

V. TYPICAL RESULTS

The model was run to simulate behavior of the flux layers above a typical 0.23 x 1.40m (9 x 54 in.) strand cast without argon at 1 m min^{-1} under the standard conditions given in Table I. The final converged velocity and thermal solutions are presented in Figures 11 - 14.

A. *Flow Field*

The most obvious feature of the flow field in Figure 11 is the large recirculation zone that extends from the SEN to about 250 mm from the narrowface. While the steel flow attempts to drag the liquid flux towards the SEN, an opposing flow carries the upper layers of flux and powder in the opposite direction. Based on the calculated size of the liquid region, this recirculation zone contains about 3.65 kg of liquid flux. This corresponds to a mean residence time of flux in the liquid pool of 112 s.

Powder flux above the recirculation zone moves slowly towards the narrowface at a velocity which increases with distance from the wideface. Figure 12 compares the velocity distribution at two positions along the top-surface with the corresponding velocity at the flux-steel interface. The maximum velocity along the top surface is only about 1.5 mms^{-1}. This slow drift towards the narrowface, away from the SEN, is consistent with the usual plant observation that powder must be added more often near the SEN, than near the narrowface.

Another significant feature of the flow field is the separation point, detailed in Figure 13. The applied shear stress along the flux steel interface increases from zero at the narrowface to its maximum of 0.26 Nm^{-2}, 0.3 m from the narrowface, and back down to zero at the SEN. This shear stress always directs flow of liquid flux towards the SEN. On the other hand, the consumption of liquid flux into the narrowface gap tends to drive liquid flux away from the SEN. At the point along the flux - steel interface where these driving forces balance, a separation in the flux flow field is produced. This separation occurs about 70 - 80 mm from the narrowface.

The flow of liquid flux is predominantly in the x-direction. Over most of the domain, flux consumption to the wideface has little effect on the flow pattern. Close to the meniscus, however, the steel flow and corresponding x-direction flux velocities diminish. Here, the consumption flow towards the mold walls is important. Figure 13 shows that flow towards the wideface dominates the flow pattern at the flow separation point. Without this flow, a shortage of liquid flux consumption and corresponding quality problems are likely. These results show that the worst potential problems should exist at the off-corner region of the wideface, for the standard conditions assumed here.

B. *Temperature Distribution*

Convective heat transport in the recirculation zone generates a much thicker liquid pool and corresponding hotter surface closer to the SEN (Figure 14). In the meniscus region, where there is no vertical (z-direction) component of flow, the liquid flux layer is thinner. However, the surface temperature close to the narrrowface is relatively high because the steel/flux interface is close to the free surface there.

Another pronounced feature of the thermal field in Figure 14 is the relatively cool top surface near the wideface wall in the off-corner region, about 150 - 250 mm from the narrowface wall. This is due to the flow separation phenomenon discussed previously. In effect, heat is being convected from that location towards the narrowface, wideface and SEN faster than it can propagate to the top of the flux by conduction. This convective removal of heat from this region leaves less heat to melt the flux, which leads to both a thinner liquid layer, and lower top-surface temperature.

C. *Flux Layer Thicknesses*

The variation in thickness of the liquid flux layer around the mold perimeter is shown in Figure 15. This thickness is very important because it controls the amount of liquid flux available to enter the gap. The solid-liquid interface was identified using the 1000°C isotherm. Convection in the recirculation zone generates the thickest liquid flux layer near the SEN, between 400 and 700 mm from the narrowface wall. Near the narrowface, the liquid flux layer is inherently thin. However ,the thinnest liquid layer is found along the wideface wall between 150 and 250 mm from the corner. This region corresponds to the flow separation point and is expected to be a generic location at which the gap may be starved for liquid flux. Its exact location should vary with casting conditions, as it depends directly on the flow pattern developed in the steel and other variables.

VI. NUMERICAL VALIDATION

Numerical studies were performed to obtain a suitable grading of the 3-D mesh. Further tests to ensure accurate mesh-independent results were performed using refined 2-D meshes, for computational reasons. The 2-D model simulates a slice through the x-z center-plane so inlet z-velocities at the top surface were reduced to incorporate flux consumption only to the narrowface. This necessary assumption for the 2-D model over-predicts liquid flux thickness, particularly at the meniscus, where heat loss via flux transport to feed consumption along the wideface is neglected. The 2-D model was otherwise similar to the 3-D model.

Using a 2-D model with the same mesh discretization in the x and z-directions as the 3-D model (440 9-node elements), the coupled problem was solved.[23] The mesh was then refined almost 16-fold (6400 9-node elements), and the analysis re-run. The maximum change in the melt interface position was only 15%, so the 3-D model mesh refinement was deemed adequate.

VII. EXPERIMENTAL VALIDATION

A. *Experimental Procedure*

The model predictions of this work were validated by measuring the depths of the powder / liquid flux and liquid flux / steel interfaces at an operating slab caster at LTV Steel, Cleveland. The inexpensive method employed (Figure 16) consists of simply lowering a wooden "nail board" into the mold. The nail board contains two rows of 7 steel nails and aluminum wire. It is kept horizontal and carefully lowered until its underside just touches the top surface of the mold powder. Each row of nails is then 80 mm from the wideface mold walls. Liquid steel coats the nails up to the flux-steel interface. At the same time, the liquid flux melts the aluminum wires to some point above the steel level. The nail board is removed after 1-3 seconds. The distance from the end of the aluminum wire to the steel level on the nail indicates the liquid flux thickness (see Figure 17). The slope of the solidified steel indicates flow direction.

Aluminum melts at approximately 660°C, while the typical flux melting point is about 1000°C. The aluminum wires that remained after extracting the board always had pointed ends. This indicates that the immersion time was too short to allow complete melting of the aluminum, and that the portion of wire that was removed was melted very quickly. Such fast melting was deemed to be the result of transient melting in a fluid temperature considerably hotter than the liquidus temperature of aluminum. Hence, it was assumed that the end of the aluminum wire indicates the location of the interface between the high-conductivity liquid flux and the low conductivity powder, rather than the 660°C isotherm.

B. *Comparison with Model Predictions*

The standard model conditions were chosen to match the conditions of the steel plant measurements. Figure 18 compares the liquid layer thickness from the model with the measurements. The model reasonably predicts the overall trend of liquid flux depth over the entire domain. Considering the crude nature of the measuring apparatus, and the many modeling assumptions, the agreement between the model and experiment is significant.

Figure 19 compares the model predictions of the location of the melt interface with those obtained experimentally at the same position. The agreement implies that the observed relatively flat interface of the liquid flux layer can be explained without gravity, which was ignored in the model. This demonstrates the importance of the recirculation pattern generated by the flowing steel, as discussed previously.

VIII. EFFECT OF PROCESS VARIABLES

Due to the massive computer requirements of the 3-D model, it was only run again to investigate the effect of liquid flux viscosity. Further parametric studies were performed using 2-D and 1-D simplifications of this model. Standard conditions (Table I) were assumed, except where mentioned otherwise.

A. *Viscosity*

The viscosity-temperature curve significantly changes with flux composition. The curve for a generally lower viscosity flux is included in Figure 7. Figure 20 shows the effect of using this lower viscosity flux on the temperature contours. Relative to that with the standard flux (Figure 14), the surface temperature for the lower viscosity flux is generally higher, and the cold region associated with the flow separation is more compressed. These differences are caused by changes in the flow field. The lower viscosity permits larger velocities to develop in the liquid, for the same steel-flow driving force at the flux-steel interface. Higher velocities generate more thermal convective mixing, so more heat is transferred from the flux-steel interface to the upper layers of the flux.

Figures 21 and 22 show the effect of viscosity on the position of the melt interface as given by the 1000°C temperature contour. In general, decreasing flux viscosity shifts the melt interface upward. The deeper liquid layer in the central region is due to the stronger re-circulating velocities and associated thermal convection that accompany the lower viscosity. The change near the meniscus is less, however, and the change near the narrowface is negligible.

Feeding to the wideface would be expected to improve with lower-viscosity powders, owing to the general increase in liquid layer depths. This finding is in apparent agreement with the frequently quoted empirical relationship of $\mu V_c = \text{Constant}$[1-3, 42], which states that a lower viscosity should be used at higher casting speeds to achieve adequate lubrication to avoid powder-related quality problems.

B. *Thermal Conductivity*

The effect of liquid flux thermal conductivity was investigated using the fine-mesh, 2-D model[23], described in section VI. Because this model over-predicts the liquid layer thickness, its predictions are interpreted relatively.

Figure 23 compares the melt interfaces for liquid thermal conductivities of 1.0 $Wm^{-1}K^{-1}$, and the standard 3.0 $Wm^{-1}K^{-1}$. A three-fold increase in thermal conductivity increases the liquid layer thickness in the central region by only 20%. This is further evidence of the importance of convection there. However, the relative importance of convection to conduction varies with position. Convection is less important near the meniscus, where the 3-fold increase in conduction roughly doubles the liquid layer thickness.

C. *1-D Steady State Model*

A simplified 1-D model was developed to further investigate the effect of process and material parameters on liquid flux layer thickness. Flux was assumed to flow uniformly downward at the consumption rate. Analytical heat balances were performed over the flux domain, accounting for latent heat evolution at the liquid-solid interface. The resulting equations (see Appendix B) were solved on a spreadsheet.

Figure 24 shows the difference between the flux melt interface locations predicted by the 3-D, 2-D and 1-D steady state models. Because the 1-D model does not properly account for convection in the liquid pool, it under-predicts the liquid layer thickness near the SEN and overpredicts it near the

meniscus. The 2-D model incorporates convection, but it over-predicts the liquid layer thickness over most of the domain because it ignores mass consumption to the wideface as discussed previously. Finally, it can be seen that the 3-D model does the best job of predicting the location of the flux melt interface, particularly at the meniscus where the 3-D effects of mass transport are most important.

Recognizing its limitations, the 1-D model was first applied to investigate the relationship between powder layer thickness and liquid layer thickness. For total flux layer thickness less than 25 mm, adding more powder improves thermal insulation and greatly increases the steady-state thickness of the liquid flux layer. As the powder layer is increased, its effect on liquid thickness lessens. For powder layer thickness greater than 75 mm, the effect on liquid thickness is small (see Figure 25)

The model was then used to examine the relative importance of several other process and material parameters on increasing the liquid flux depth. Specific findings of this model, for the standard operating conditions in Table I, and for a reference powder layer thickness of 5 cm, include:

(i) A decrease in the melting point from 1000°C to 900°C increases the liquid layer thickness by 20%. This is illustrated in Figure 25.

(ii) Halving the consumption rate doubles the liquid thickness.

(iii) Increasing the liquid thermal conductivity from 2 to 3 $Wm^{-1}K^{-1}$ increases the liquid thickness by 50%. This proportional increase is roughly consistent with the effect of thermal conductivity in the meniscus region as calculated by the 2-D model.

(iv) Halving the powder thermal conductivity increases the liquid thickness by less than 20%.

(v) Decreasing the latent heat by 67% increases the liquid thickness by 38%.

(vi) Powder emissivity at the top surface has a negligible effect on the liquid thickness.

IX. 1-D TRANSIENT MODEL

A. *Model Formulation*

Many previous researchers have measured and referred to the "melting rate" of a flux, to characterize its melting behavior. This work instead characterizes the melting behavior of the flux using the more fundamental properties of thermal conductivity, enthalpy, and viscosity. Assuming that the melting rate is simply a manifestation of the more fundamental material properties, the present modeling approach should also be capable of calculating a "melting rate" for continuous casting operating conditions.

To investigate the transient melting behavior of the flux, a 1-D transient finite element model was formulated. The model simulates a thin strip through the flux. By including the transient term and neglecting the x and y terms, the energy conservation equation becomes:

$$\rho C_p \left[\frac{\partial T}{\partial t} + u_z \frac{\partial T}{\partial z} \right] = \frac{\partial}{\partial z} \left(k(T) \frac{\partial T}{\partial z} \right) \qquad [5]$$

The mass and momentum equations simplify to give a constant velocity in the z-direction, which must be imposed. Using the same standard input material properties and applicable boundary condition (e.g. 1550°C at steel/flux interface) as in the 2-D and 3-D models, the above non-linear

equation was solved using FIDAP. Flux temperature was calculated using an implicit time integration scheme.

B. ***Typical Results***

Predicted growth of the liquid layer thickness with time is shown in Figure 26. The melt interface (indicated by the 1000°C isotherm) is seen to reach equilibrium after about 120 minutes with zero flux consumption. The melting "speed" decreases from 0.0230 mms^{-1} at t = 1 minute, to 0.005 mms^{-1} at t = 25 minutes to 0.0005 mms^{-1} at t = 60 minutes, according to the tangent of the no-consumption curve in Figure 26. These values are comparable with the experimental melting rates from Figure 27, based on data obtained by Xie *et. al.*[6]. For the 3.8% content of the flux studied in this present work, the melting rate should be approximately 0.01 $kgm^{-2}s^{-1}$ from Figure 27. This melting rate corresponds to a melting speed of 0.004 mms^{-1} or 0.08 kg/(tonne of steel). This experimental melting speed corresponds to that computed at t = 27 minutes in Figure 26.

Further, Figure 27 shows that melting rate is a strong function of carbon content in the flux. This effect is likely due to an increase in the maximum of the apparent viscosity curve (Figure 7) at the flux / powder interface, with increasing carbon content. This is caused by carbon particles floating on the liquid layer and coating the sintering flux, and is affected strongly by the carbon particle size. The result is a decrease in both melting rate and steady liquid layer thickness with increasing carbon. A second phenomenon explaining this trend is the increased apparent latent heat of the flux with increasing carbon content, due to the endothermic reaction to form CO_2 and CaO from $CaCO_3$.

The transient 1-D model was re-run for a specific consumption of 0.4 kg/(tonne of steel) to match the conditions Nakano[19] for a casting speed of 1.5 m/min. Figure 26 illustrates the effect of imposing this consumption rate on the transient response. The time to achieve steady state is seen to decrease to 25 minutes, which is close to that predicted by Nakano. The drop in melting rate with time is even more pronounced. It should be noted that the Nakano model uses a sintering model to define the thermal conductivity and specific heat for the different forms of the flux, while the model presented here uses average empirical data for these properties as functions of temperature.

C. ***Evaluation of Steady-State Assumption***

Based on the results of the previous section, it seems reasonable that "quasi" steady state liquid levels can be approached in practice. Nakano and co-workers[19] validated this concept by taking measurements of liquid layer depth at an operating caster. Their results show that the pool thickness exhibits a nearly constant value, which varies with casting parameters. The intermittent addition of powder was modeled by Dehalle et. al.[18] and predicted to have no significant effect on the liquid layer thickness, once the "quasi" steady-state is achieved. However, Figure 28 schematically presents the typical variations in the liquid layer thickness expected under these quasi-steady state conditions.

The flux thickness data points in Figure 28 were measured at LTV steel at the quarter width along the mold centerline for a casting speed of 1.07 m/min. The predicted 1-D steady-state liquid flux thickness (2.1 cm) was taken from Figure 25. Figure 28 shows that with intermittent powder addition, the liquid flux thickness probably varies about a mean quasi-steady value, which may be less than the

steady-state value predicted with a constant rate of powder addition. The difference between the quasi-steady and steady values arises because the typical time interval between powder additions (on the order of 3 minutes) is so much less than the time needed to reach steady state (about 25 minutes). There is not enough time for the full steady-state liquid thickness to develop. Based on the same argument, the time is sufficiently short that the fluctuation in liquid depth is not significant, so the quasi-steady state assumption appears to be reasonable. These results imply that the true liquid layer thickness should be smaller than that predicted by the steady state models.

X. CONCLUSIONS

A 3-D steady-state coupled fluid flow and heat-transfer finite-element model has been formulated to calculate the velocity and thermal fields developed in the top-surface flux layers in a continuous steel slab-casting mold under typical operating conditions. The model includes different temperature-dependent functions for viscosity and thermal conductivity in regions of melting and solidifying of the flux. The model calculations roughly agree with measured flux layer thicknesses in an operating slab casting mold, for a typical recirculating steel flow pattern with surface flow directed back towards the SEN. Specific findings of the model include:

1. Flow in the meniscus region is essentially planar, normal to the direction of maximum heat flux. Therefore heat transfer in this region is controlled by conduction and latent heat of the flux, and the liquid flux layer is thin.
2. Due to steel flow dragging flux along the interface, a large recirculation zone develops in the central region of the flux. This increases convection, causing a deeper liquid layer near the SEN. The result is an almost flat top surface of the liquid flux layer, despite an uneven steel surface and despite ignoring the effect of gravity in the model.
3. Recirculating flow carries powder towards the narrowface walls, opposite to the direction of steel flow. This implies that more powder must be added at the center near the SEN, even if consumption around the mold perimeter is uniform.
4. Flow separation in the flux layer, between 150 and 250 mm from the narrow face, results in a very thin liquid layer. This may result in poor feeding of liquid flux into the mold-strand gap, particularly at the off-corner region of the wideface. Thin flux layers and feeding problems are also generic near the narrow face in general.
5. A cold spot develops along the wideface wall about 150 mm from the narrow face. This is associated with a thin liquid flux layer, and low heat loss through the flux. This suggests a thicker resolidified flux rim and generally worse quality problems might exist there.
6. Viscosity plays an important role in the thermal and flow behavior of the flux. Lower liquid-flux viscosity produces thicker liquid layers in the deep central flux pool in the mold, due to better convective mixing. This may contribute to the higher consumption and better quality-performance of low viscosity flux.

7. Changes in liquid flux viscosity have little effect on the liquid layer thickness near the meniscus of the narrowface.
8. For total flux layer thicknesses less than 25 mm, adding more powder significantly increases the depth of the liquid flux layer. As the powder layer depth increases, this effect lessens, and for powder layer thicknesses greater than 75 mm, the effect on liquid layer thickness is small.
9. This work has shown that steel flow in the mold controls the liquid flux layer thickness profile. Thus, changes to the mold flow pattern will affect the liquid flux layer thickness, which in turn will affect steel quality.

APPENDIX

A. *Input Velocities*

Average vertical velocity into top surface $= \dfrac{m_{sc}\, V_c\, (w_m + t_m)}{\rho (w_m T_m)}$

$= 4.071 \times 10^{-5}$ m s^{-1}

Consumption velocity to wide face $= \dfrac{m_{sc}\, V_c\, w_m}{4 \rho A_{exit}}$

$= 0.000953$ m s^{-1}

where: A_{exit} = Area of outlet to wideface $= 0.294 \times 10^{-2}$ m^2

B. *1-D Model Equations*

$$T_{surf} = \frac{k_p T_{fmelt} + h_{tot}\, w_p T_{amb}}{h_{tot} w_p + k_p} \qquad [B1]$$

$$w_f = \frac{k_f A (T_{st} - T_{f,melt}) w_p}{\left[k_p A (T_{f,melt} - T_{surf}) + w_p \dot{m}_c \Delta H_L \right]} \qquad [B2]$$

$$h_{eff} = \left[\sigma \varepsilon (T_{surf} + T_{amb})(T_{surf}^2 + T_{amb}^2) \right] + \frac{5}{3} \left\{ \frac{0.5013 k_{air}^{3/4} \left(C_p \mu \right)^{1/4} \left[g \beta (T_{surf} - T_{amb}) \right]^{1/5}}{\nu^{2/5} D^{2/5}} \right\} \qquad [B3]$$

ACKNOWLEDGMENTS

The authors wish to thank the steel companies: Armco, Inc. (Middletown, OH), Inland Steel Corporation (East Chicago, IN), LTV Steel (Cleveland, OH) and BHP Co. Ltd. (Wallsend, Australia) for grants which made this research possible and particularly Bill Emling and Lee Hendrix at LTV for providing facilities and assistance with collection of experimental data. This work is also supported by the National Science Foundation under grant No. MSS - 8957195. The authors also wish to acknowledge Fluid Dynamics Inc. for assistance with the FIDAP program and to the National Center for Supercomputing Applications at the University of Illinois at Urbana-Champaign for time on the Cray Y-MP supercomputer.

TABLE I. SIMULATION CONDITIONS AND NOMENCLATURE

Symbol	Variable	Value
C_p	specific heat of flux, $Jkg^{-1}K^{-1}$	see Fig. 9
d_g	mold-strand gap thickness in simulation domain, m	0.0008
g	acceleration due to gravity, ms^{-2}	9.81
h_c	convective heat transfer coefficient	
h_{conv}	effective natural convective heat transfer coefficient, $Wm^{-2}K^{-1}$	see Fig. 6
h_{eff}	effective total heat transfer coefficient, $Wm^{-2}K^{-1}$	see Fig. 6
h_{rad}	effective radiative heat transfer coefficient, $Wm^{-2}K^{-1}$	see Fig. 6
k_p , k_f	powder flux, liquid flux thermal conductivity, $Wm^{-1}K^{-1}$	see Fig. 8
l_g	mold-strand gap length in simulation domain, m	0.027
L_h	Equivalent Hydraulic diameter of mold, m ($= \sqrt{(w_m\ t_m)}$)	0.2829
m_{sc}	flux specific consumption, kgm^{-2}	0.6
$\dot{m}_c$	flux consumption rate, kgs^{-1}	0.0326
$\dot{M}_c$	flux consumption per meter of mold perimeter, $kgm^{-1}s^{-1}$	0.0100
N	number of nodes	28,500
P	pressure, Nm^{-2}	
q_n	normal heat flux, Wm^{-2}	
t_m	half-mold thickness, m	0.1143
T	temperature, °C	
T_{amb}	ambient temperature, °C	30
$T_{f,melt}$	flux melting temperature, °C	1000
$T_{f,s}$	flux sintering temperature, °C	900
T_{st}	molten steel surface temperature, °C	1550
T_{surf}	surface temperature of flux, °C	
u_x, u_y, u_z	velocity components in x, y and z -directions, ms^{-1}	
v	Characteristic velocity of liquid flux, ms^{-1}	
V_c	casting speed, ms^{-1}	0.0166
w_p ,w_f	powder flux, liquid flux layer thickness, m	
w_m	half-mold width, m	0.7
x	coordinate in mold width direction, m	
X_f	total flux thickness, m	
$X_{f,max}$	maximum total flux thickness, m	0.035
$X_{f,men}$	total flux thickness at meniscus, m	0.01
$X_{f,SEN}$	total flux thickness at SEN, m	0.027
y	coordinate in mold thickness direction, m	
z	coordinate in negative casting direction, m	
ΔH_L	enthalpy of fusion, $kJkg^{-1}$	350
ΔT	Characteristic temperature difference for natural convection, K	650
β	Volumetric expansion of liquid flux, K^{-1}	2.4×10^{-5}
ε_{fl}	flux emissivity	0.7
γ_{st}	surface tension for liquid steel in air[26], Nm^{-1}	1.6
μ	kinetic viscosity of flux, $kgm^{-1}s^{-1}$	see Fig. 7
μ_{st}	kinetic viscosity of steel at liquidus, $kgm^{-1}s^{-1}$	0.0055
ρ	density of flux, kgm^{-3}	2500
ρ_{st}	density of steel, kgm^{-3}	7800
σ	Stefan-Boltzmann constant, $Wm^{-2}K^{-4}$	5.667×10^{-8}
τ	shear stress, Nm^{-2}	

TABLE I - CONTINUED

Symbol	Variable	Value
Re	Reynolds Number $\left(= \frac{\rho_{st} v L_h}{\mu} \right)$	70
Fr*	Modified Froude Number $\left(= \frac{v^2}{g X_{f\text{-}max} \beta \Delta T} \right)$	0.077
Br	Brinkman Number $\left(= \frac{\mu v^2}{k \Delta T} \right)$	6.0×10^{-9}
Gr	Grashof Number $\left(= \frac{\rho^2 g \beta \Delta T L^3}{\mu^2} \right)$	80
We	Weber Number $\left(= \frac{\rho v^2 L_h}{\gamma_{st}} \right)$	1.5×10^{-3}

TABLE II - SOLUTION PARAMETERS FOR 3-D MODEL

Problem Type	Relaxation Factor	RCONV.	Disk Space (MB)	Total Number of Iterations	Total Solution Time (CPUs)†
Isothermal Flow	None	0.001	990	5	3500
Energy (Adv-Diff)	0.4	0.01	59	110	4320
Coupled	0.3	0.01	1,800	45	67,500

† *CPU - seconds on the CRAY Y-MP using 8MW RAM*

REFERENCES

1. Ogibayashi, S., Yamaguchi, K., Mukai, T., Takahashi, T., Mimura, Y. and Koyama, K.: "Mold Powder Technology for Continuous Casting of Low Carbon Aluminum-killed Steel", *Nippon Steel Technical Report,* 1987, vol. 34 (7), pp. 1 - 10.

2. Nakano, T., Kishi, T., Koyama, K., Komai, T. and Naitoh, S.: "Mold Powder Technology for Continuous Casting of Aluminum-killed Steels", *Transactions ISIJ,* 1984, vol. 24 (11), pp. 950 - 956.

3. Bommaraju, R.: "Optimum Selection and Application of Mold Fluxes for Carbon Steels", *Steelmaking Conference Proceedings*, Iron and Steel Society of AIME, Warrendale, PA, 1991, Vol. 74, pp. 131 - 146.

4. Sardemann, J. and Schrewe, H.: "The Influence of Casting Powder on the Formation of Cracks in Continuous Slab Casting", *Steelmaking Conference*, Iron and Steel Society of AIME, Warrendale, PA, 1991, Vol. 74, pp. 719 - 729.

5. Nakato, H., Takeuchi, S., Fujii, T., Nozaki, T. and Washio, M.: "Characteristics of New Mold Fluxes for Strand Casting of Low and Ultra Low Carbon Steel Slabs", *Steelmaking Conference Proceedings*, Iron and Steel Society of AIME, Warrendale, PA, 1991, Vol. 74, pp. 639 - 646.

6. Xie, B., Wu, J. and Gan, Y.: "Study on Amount and Scheme of Carbon Mixed in Continuous Casting Mold Fluxes", *Steelmaking Conference Proceedings*, Iron and Steel Society of AIME, Warrendale, PA, 1991, Vol. 74, pp. 647 - 651.

7. Branion, R.V.: "Mold Fluxes for Continuous Casting", *Steelmaking Conference Proceedings*, Iron and Steel Society of AIME, Warrendale, PA, 1986, Vol. 69, pp. 95 - 105.

8. Moore, J.A., Phillips, R.J. and Gibbs, T.R.: "An Overview for the Requirements of Continuous Casting Mold Fluxes", *Steelmaking Conference Proceedings*, Iron and Steel Society of AIME, Warrendale, PA, 1991, Vol. 74, pp. 615 - 621.

9. Lindefelt, H. and Hasselstrom, P.: *4th International Iron and Steel Congress*, The Metals Society, 1982, pp. 23 - 31.

10. Bommaraju, R. and Saad, E.: "Mathematical Modeling of Lubrication Capacity of Mold Fluxes", *Steelmaking Conference Proceedings*, Iron and Steel Society of AIME, Warrendale, PA, 1990, Vol. 73, pp. 281 - 296.

11. Machingawuta, N.C., Bagha, S. and Grievson, P.: "Heat Transfer Simulation for Continuous Casting", *Steelmaking Conference Proceedings*, Iron and Steel Society of AIME, Warrendale, PA, 1991, Vol. 74, pp. 163.

12. Thompson, K.J.: "Optimizing Slag Performance in the Mould", *Steelmaking Conference Proceedings,* 1989, vol. 72, pp. 109 - 114.

13. Nakato, H., Sakuraya, T., Nozaki, T., Emi, T. and Nishikawa, H.: "Physical and Chemical Properties of Casting Powders affecting the Mold Lubrication during Continuous Casting", *Steelmaking Conference Proceedings*, Iron and Steel Society of AIME, Warrendale, PA, 1986, Vol. 69, pp. 137 - 143.

14. Anzai, E., Ando, T., Shigezumi, T., Ikeda, M. and Nakano, T.: "Hydrodynamic Behavior of Molten Powder in Meniscus Zone of Continuous Casting Mold", *Nippon Steel Technical Report,* 1987, vol. 34 (7), pp. 31 - 40.

15. Yamauchi, A., Sorimachi, K., Sakuraya, T. and Fujii, T.: "Heat Transfer between Mold and Strand through Mold Flux Flim in Continuous Casting of Steel", *ISIJ International,* 1993, vol. 33 (1), pp. 140 - 1147.

16. Ohmiya, S., Tacke, K.-H. and Schwerdtfeger, K.: "Heat Transfer Through Layers of Casting Fluxes", *Ironmaking and Steelmaking,* 1983, vol. 10 (1), pp. 24 - 30.

17. Ho, B.: *Characterization of Interfacial Heat Transfer in the Continuous Slab Casting Process*, Masters Thesis, University of Illinois at Urbana-Champaign, 1991.

18. Delhalle, A., Larrecq, M., Marioton, J.F. and Riboud, P.V.: "Slag Melting and Behavior at Meniscus Level in a Continuous Casting Mold", *Steelmaking Conference Proceedings*, Iron and Steel Society of AIME, Warrendale, PA, 1986, Vol. 68, pp. 145 - 152.

19. Nakano, T., Fuji, M., Nagano, K., Matsuyama, T. and Masuo, N.: "Model Analysis of Melting Process of Mold Powder for Continuous Casting of Steel", *Nippon Steel Technical Report,* 1987, vol. 34 (7), pp. 21 - 30.

20. Chui, G.K. and Gardon, R.: "Interaction of Radiation and Conduction in Glass", *Journal of the American Ceramic Society,* 1969, vol. 52 (10), pp. 548 - 553.

21. Taylor, R. and K.C., M.: "Physical Porperties of Casting Powders: Part 3 - Thermal Conductivities of Casting Powders", *Ironmaking and Steelmaking,* 1988, vol. 15 (4), pp. 187 - 194.

22. Mikrovas, A.C., Argyropoulos, S.A. and Sommerville, I.D.: "Measurements of the Effective Thermal Conductivity of Liquid Slags", *Iron and Steelmaker,* 1991, vol. 18 (12), pp. 51 - 61.

23. McDavid, R.M.: *Fluid Flow and Heat Transfer Behavior of Top-Surface Flux Layers in Steel Continous Casting*, M.Sc. Thesis, University of Illinois at Urbana-Champaign, 1994.

24. Huang, X. *Personal Communication*. 1993.

25. Huang, X., Thomas, B.G. and Najjar, F.M.: "Modeling Superheat Removal during Continuous Casting of Steel Slabs", *Metallurgical Transactions B,* 1992, vol. 23 (6), pp. 339-355.

26. Jimbo, I., Ozturk, B., Feldbauer, S. and Cramb, A.W.: "Some Aspects of Chemical Phenomena in the Mold of a Continuous Slab Caster", *Steelmaking Conference Proceedings*, Iron and Steel Society of AIME, Warrendale, PA, 1991, Vol. 74, pp. 117 - 126.

27. Tomono, H., Kurz, W. and Heinemann, W.: "The Liquid Steel Meniscus in Molds and its Relevance to the Surface Quality of Castings", *Metallurgical Transactions B,* 1981, vol. 12, pp. 409 - 411.

28. Lanyi, M.D. and Rosa, C.J.: "Viscosity of Casting Fluxes Used During Continuous Casting of Steel", *Metallurgical Transactions B,* 1981, vol. 12 (6), pp. 287 - 297.

29. McCauley, W.L. and Apelian, D.: "Temperature Dependence of the Viscosity of Liquids", *Proceedings of 2nd International Symposium on Metallurgical Slags and Fluxes*, H.A. Fine and D.R. Gaskell, eds., Metallurgical Society of AIME, Warrendale, PA, 1984, pp. 925 - 947.

30. Woodruff, H.C.: "Rheological Properties of Plastic-Mineral Composite Powders Affecting Fluidization and Air Transport", *Powder Technology,* 1973, vol. 8, pp. 283-291.

31. Matheson, G.L., Herbst, W.A. and Holt, P.H.: "Fluid-Solid Systems", *Industrial and Engineering Chemistry,* 1949, vol. 41, pp. 1099.

32. Ashwin, B.S., Hagyard, T., I.C.B., S. and Young, T.E.: "Viscometers Having Damped Torsional Oscillation", *Journal of Scientific Instruments,* 1960, vol. 37, pp. 480 - 485.

33. Botterill, J.S.M., Van der Kolk, M., Elliot, D.E. and McGuigan, S.: "The Flow of Fluidized Solids", *Powder Technology,* 1972, vol. 6, pp. 343 - 351.

34. Reitema, K.: *The Dynamics of Fine Powders: Rheology of Fluidized Powders (Chapter 9)*, Elsevier Science, New York, 1991, pp. 162 - 186.

35. Adewumi, M.A., Arastoopour, H.: "Two Dimensional Steady State Hydrodynamics Analysis of Gas-Solids Flow in Vertical Pneumatic Conveying Systems", *World Congress Particle Technology*, K. Leschonski, eds., NMA Nürnberger Messe- und Austellungsgesselschaft mbH, 1986, Vol. Part III: Mechanics of Particulate Solids Pneumatic and Hydraulic Conveying Mixing, pp. 351 - 386.

36. Arastoopour, H. and Cutchin III, J.H.: "Measurement and Analyis of Particle-Particle Interaction in a Co-current Flow of Particles in a Dilute Gas-Solid System", *Chemical Engineering Science,* 1985, vol. 40 (7), pp. 1135 - 1143.

37. Kishimoto, M., Maeda, M., Mori, K. and Kawai, Y.: "Thermal Conductivity and Specific Heat of Metallurgical Slags", *Proceedings of 2nd International Symposium on Metallurgical Slags and Fluxes*, H.A. Fine and D.R. Gaskell, eds., Metallurgical Society of AIME, Warrendale, PA, 1984, pp. 891 - 905.

38. Nagata, K., Susa, M. and Goto, K.S.: "Thermal Conductivities of Slags for Ironmakng and Steelmaking", *Transactions of the ISIJ (Tetsu-to-Hagane),* 1983, vol. 69, pp. 1417 - 1424.

39. Nagata, K. and Goto, K.S.: "Heat Conductivity and Mean Free Path of Phonons in Metallurgical Slags", *International Symposium on Metallurgical Slags and Fluxes*, H.A. Fine and O.R. Gaskell, eds., Metallurgical Society of AIME, Warrendale, PA, 1984, pp. 875 - 889.

40. Ponsford, F.H., Mills, K.C., Grievson, P., Canham, D.L. and Broadbent, C.P.: "Physical and Thermal Properties of Aluminate Slags", *3rd International Conference on Molten Slags and Fluxes*, 1988, pp. 332 - 335.

41. Engleman, M.S.: *FIDAP Theoretical Manual - Revision 6.0*, Fluid Dynamics International, Inc., Evanston, IL, 1991, pp. 3.1 - 3.4.

42. Koyama, K., Nagano, K. and Nakano, T.: “Design for Chemcial and Physical Properties of Continuous Casting Powders”, *Nippon Steel Technical Report,* 1987, vol. 34 (7), pp. 41 - 47.

43. Kakaç, S., Shah, R.K. and Aung, W.: *Handbook of Single-Phase Convective Heat Transfer*, John Wiley & Sons, New York, 1987, pp. 1.21 - 1.35.

LIST OF FIGURES

Figure 1: Schematic showing physical interation of flux and steel in a continuous slab casting mold
Figure 2: Schematic of continuos slab casting mold, showing flux simulation domain
Figure 3: Dimensions of simulation domain (in meters)
Figure 4: Flow Boundary Conditions
Figure 5: Velocities in steel calculated by 3-D flow model[24]
Figure 6: Thermal Boundary Conditions
Figure 7: Viscosity-temperature models for melting and solidifying of two different fluxes
Figure 8: Thermal conductivity-temperature model for melting and solidifying flux
Figure 9: Enthalpy-temperature model for flux
Figure 10: Flow chart of model solution methodology
Figure 11: Calculated velocity distribution in flux layers at top surface and at mid-plane showing recirculation zone and flow separation (standard conditions)
Figure 12: Top-surface and flux/steel interface velocity distribution as function of distance from narrowface
Figure 13: Calculated velocity distribution at flux/steel interface and at mid-plane shown flow separation and recirculation (standard conditions)
Figure 14: 3-D Temperature distribution calculated in flux layer (°C, standard conditions)
Figure 15: Liquid layer thickness around mold perimeter (standard conditions)
Figure 16: Schematic of layer thickness meanurement method
Figure 17: Close-up of cross-section through “nail-board”
Figure 18: Comparison of measured and predicted liquid layer thicknesses
Figure 19: Comparison of measured and predicted melt-interface positions
Figure 20: 3-D temperature distribution calculated for flux with lower liquid viscosity (temperatures in °C).
Figure 21: Effect of viscosity on average position of melt interface
Figure 22: Position of melt interface at several locations in the mold as a function of liquid flux viscosity
Figure 23: Effect of liquid thermal conductivity on location of melt interface
Figure 24: Comparison of prediction of melt interface location for 1-D, 2-D and 3-D models
Figure 25: 1-D prediction of relationship between powder layer thickness and liquid layer thickness as a function of the flux melting temperature
Figure 26: Effect of liquid flux consumption on time taken to achieve steady state
Figure 27: Effect of carbon content on Melting rate of flux
Figure 28: Transient schematic showing a possible effect of intermittent powder addition. The points are typical measuremts at the mold center-plane and quarter width

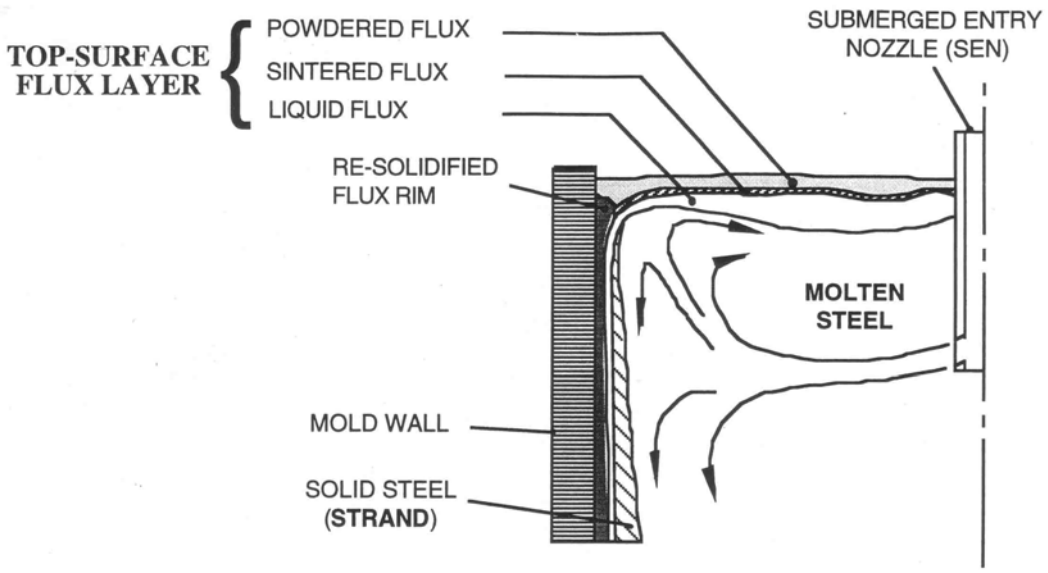

Figure 1: Schematic showing physical interaction of flux and steel in continuous slab-casting mold

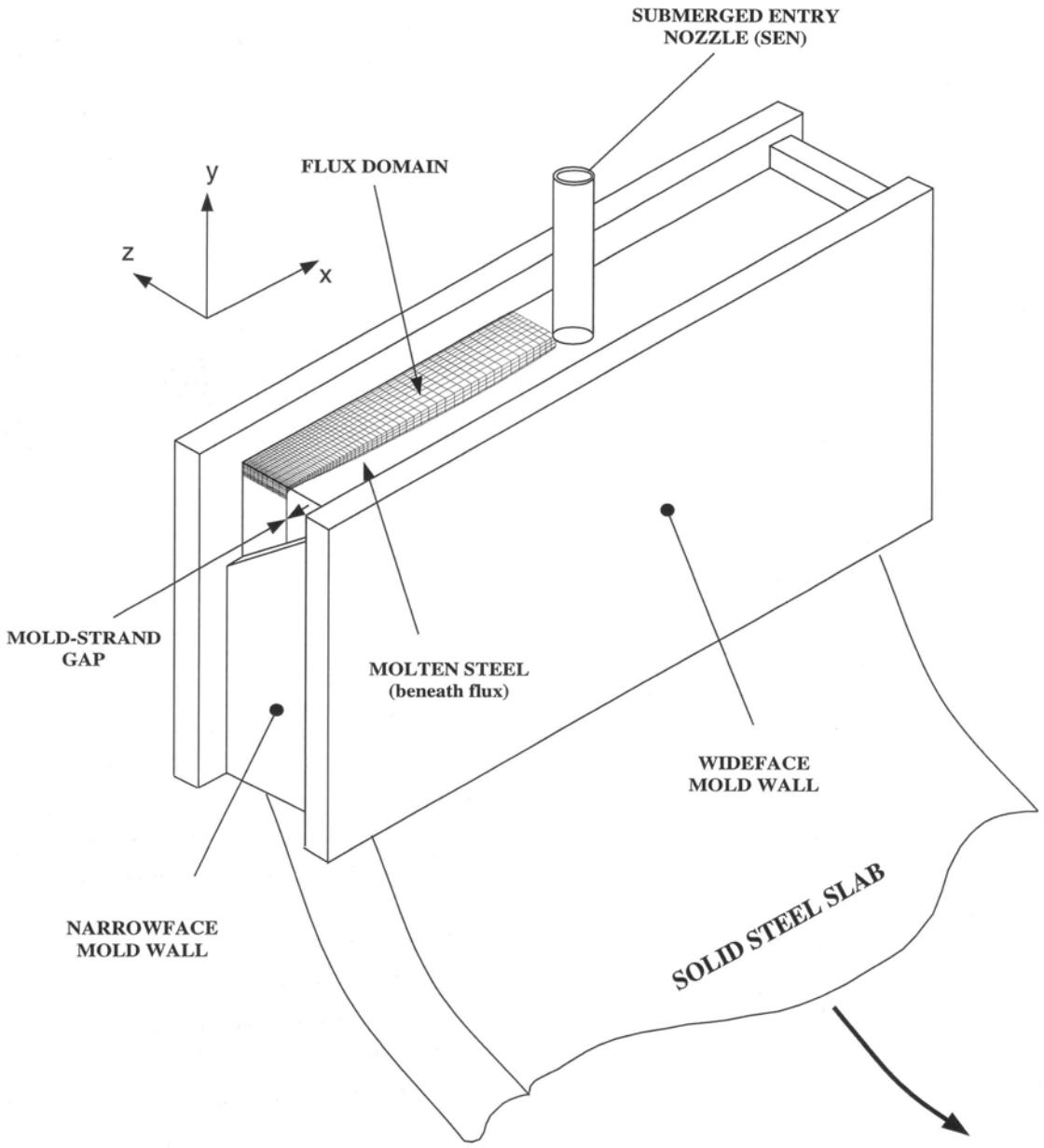

Figure 2: Schematic of continuous slab casting mold, showing flux simulation domain

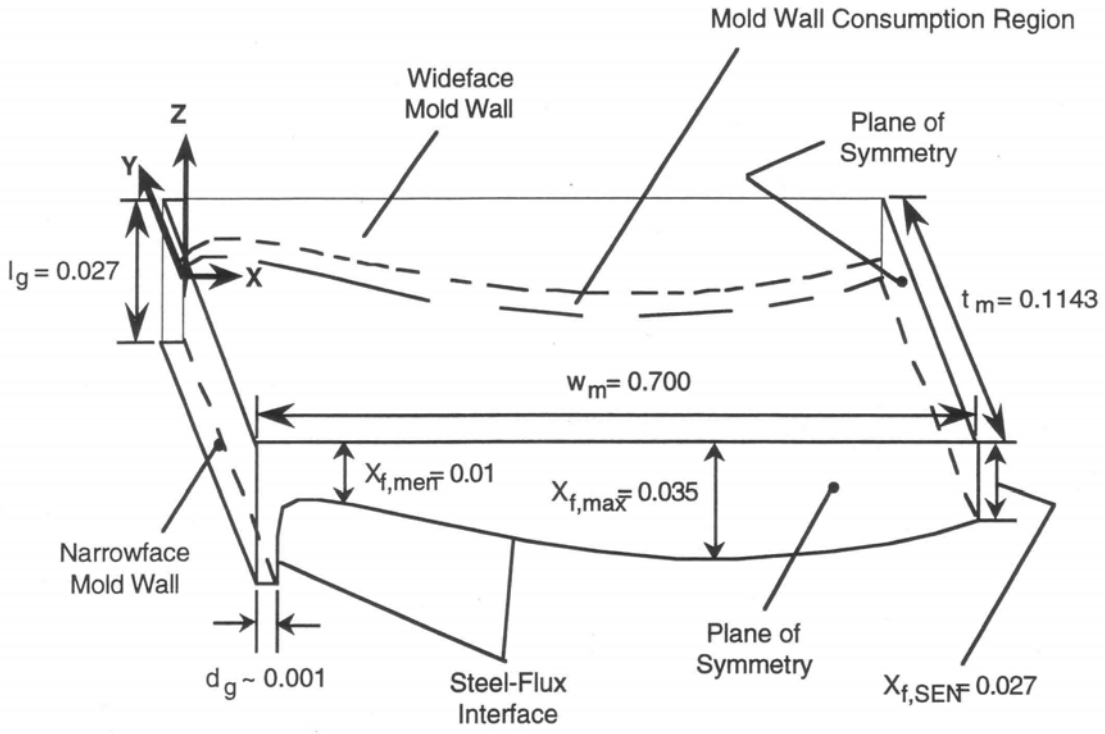

Figure 3: Dimensions of simulation domain (in meters)

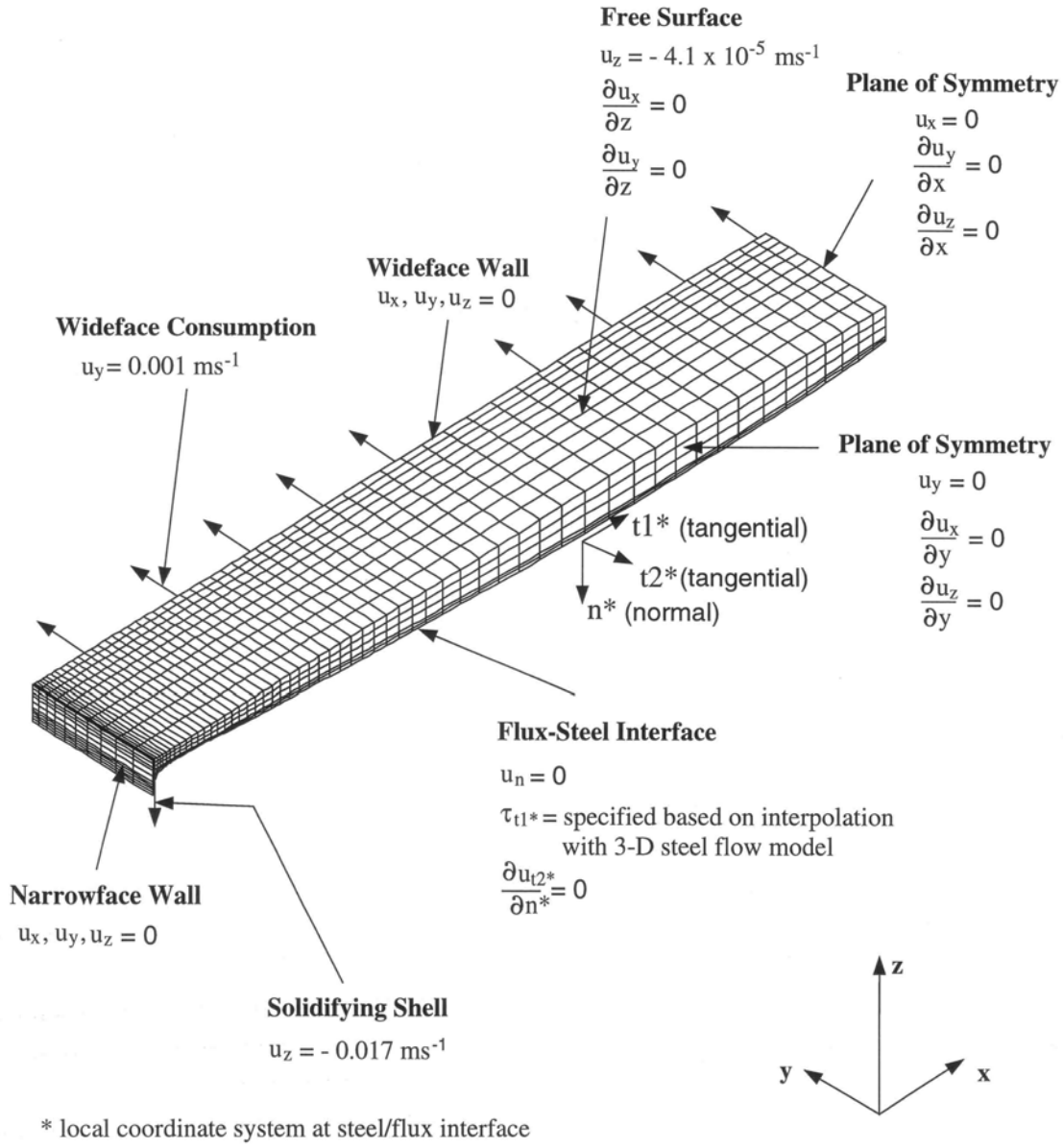

Figure 4: Flow Boundary Conditions

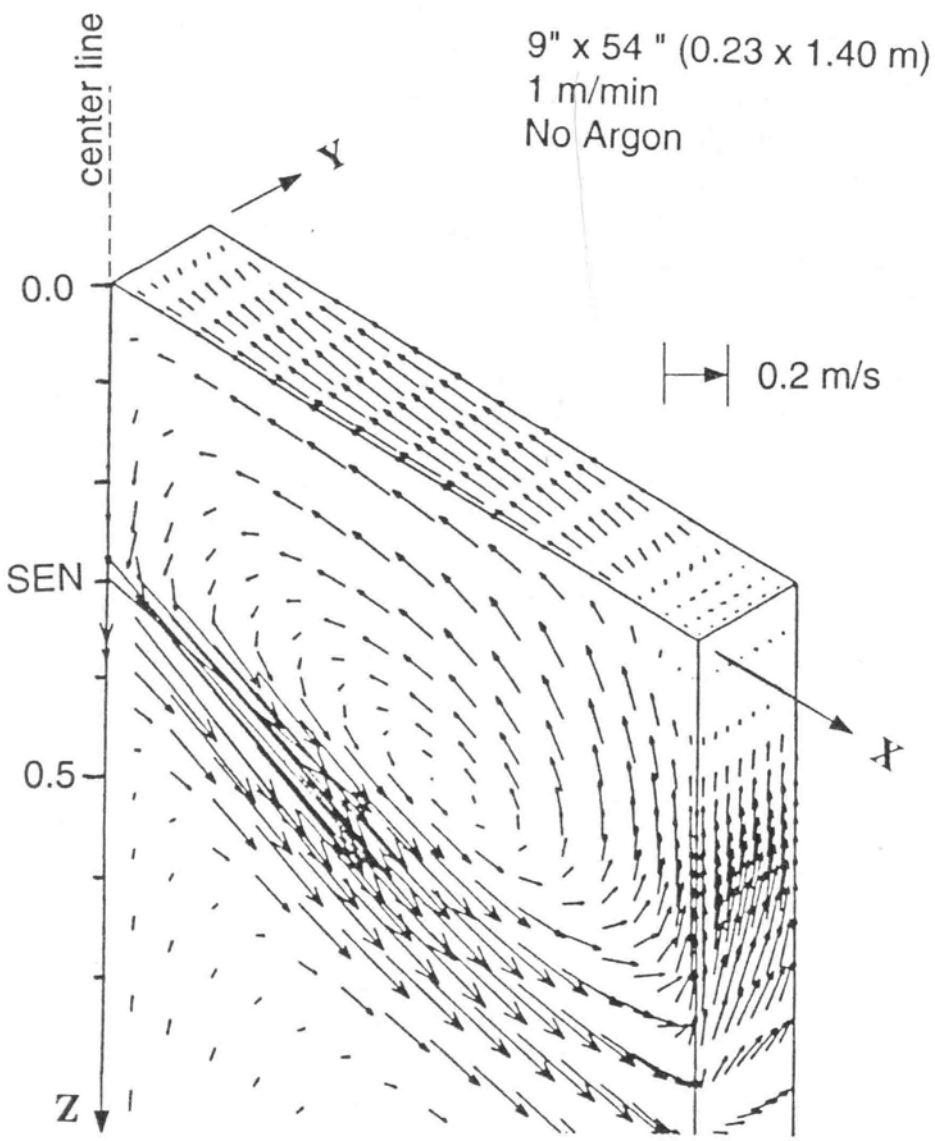

Figure 5: Velocities in steel calculated by 3-D flow model [24]

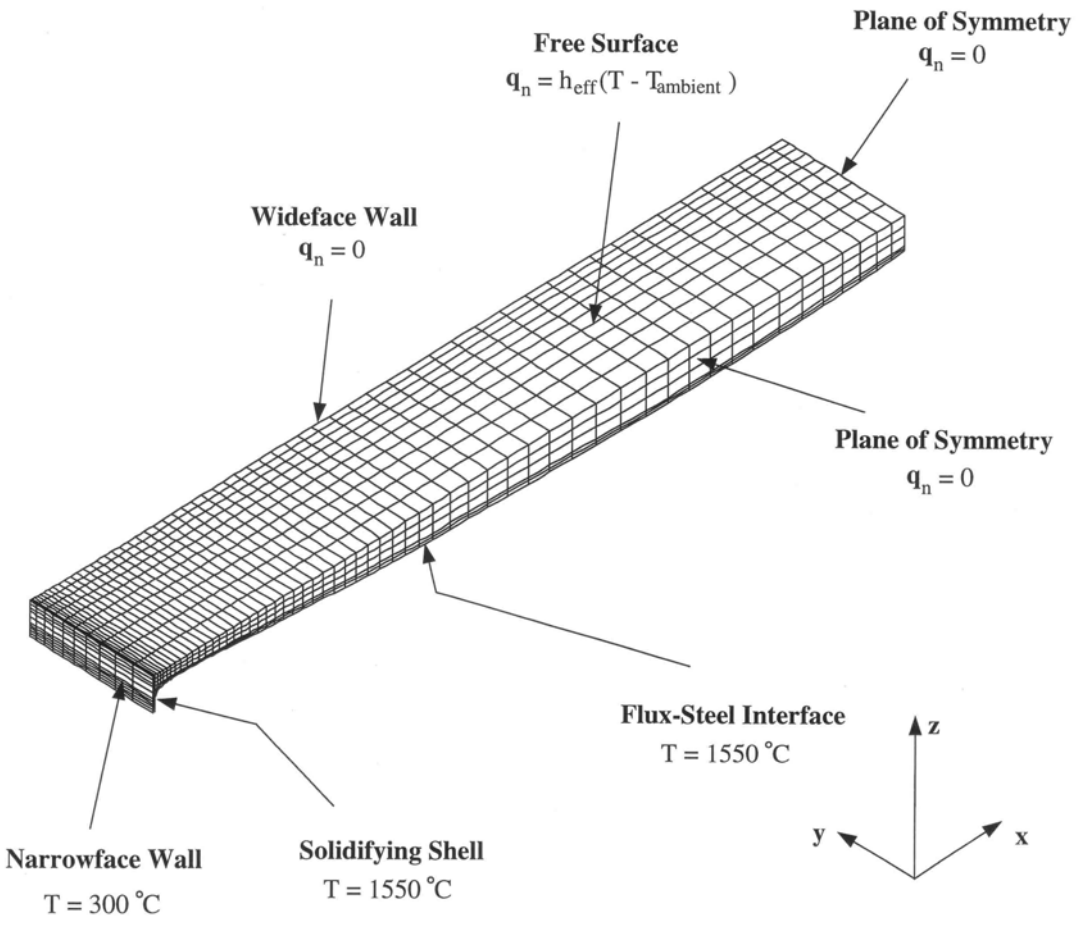

Figure 6: Thermal Boundary Conditions

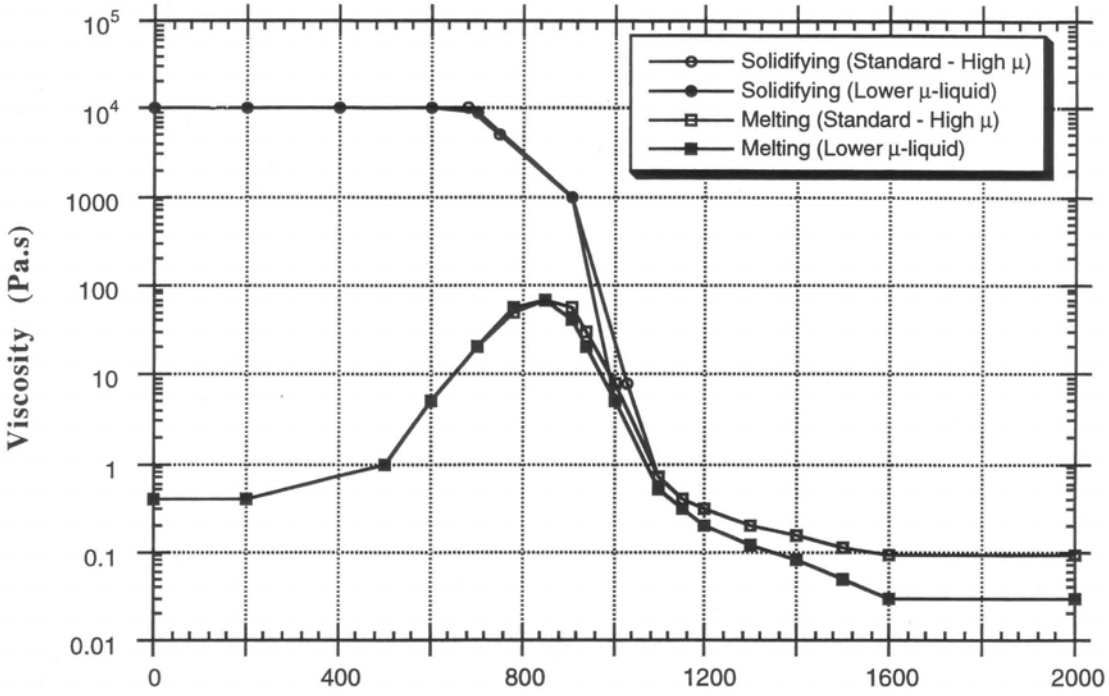

Figure 7: Viscosity-Temperature Models for Melting and Solidifying of two different fluxes

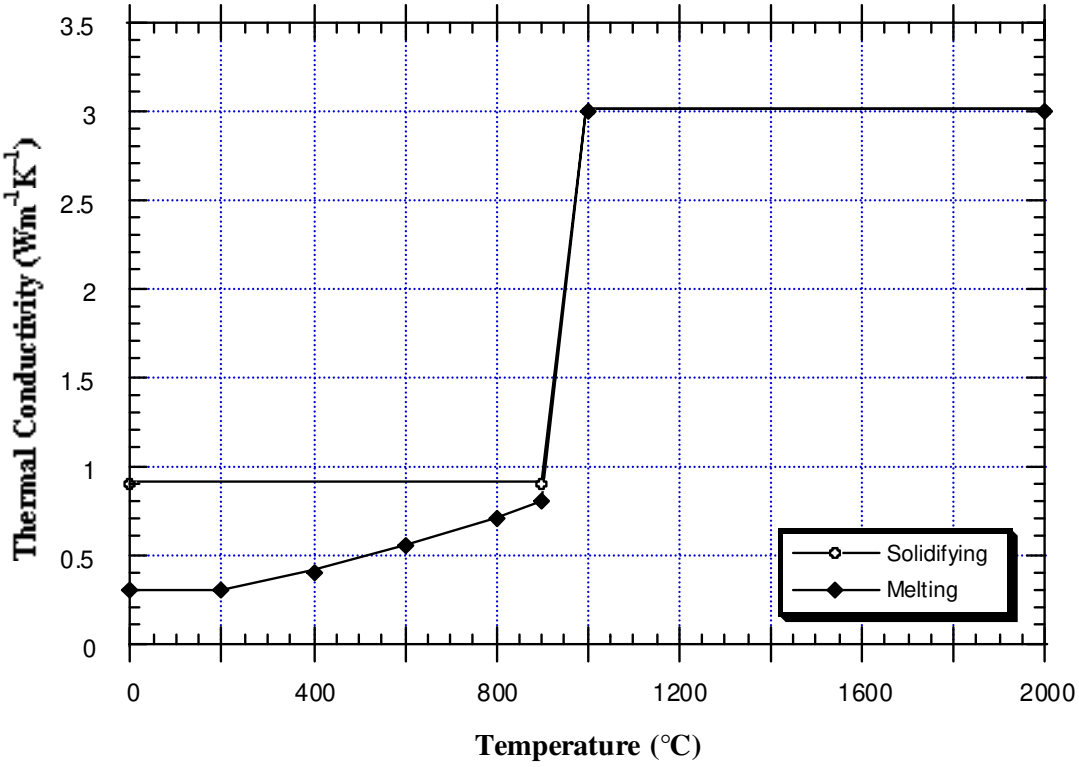

Figure 8: Thermal conductivity-temperature model for melting and solidifying flux

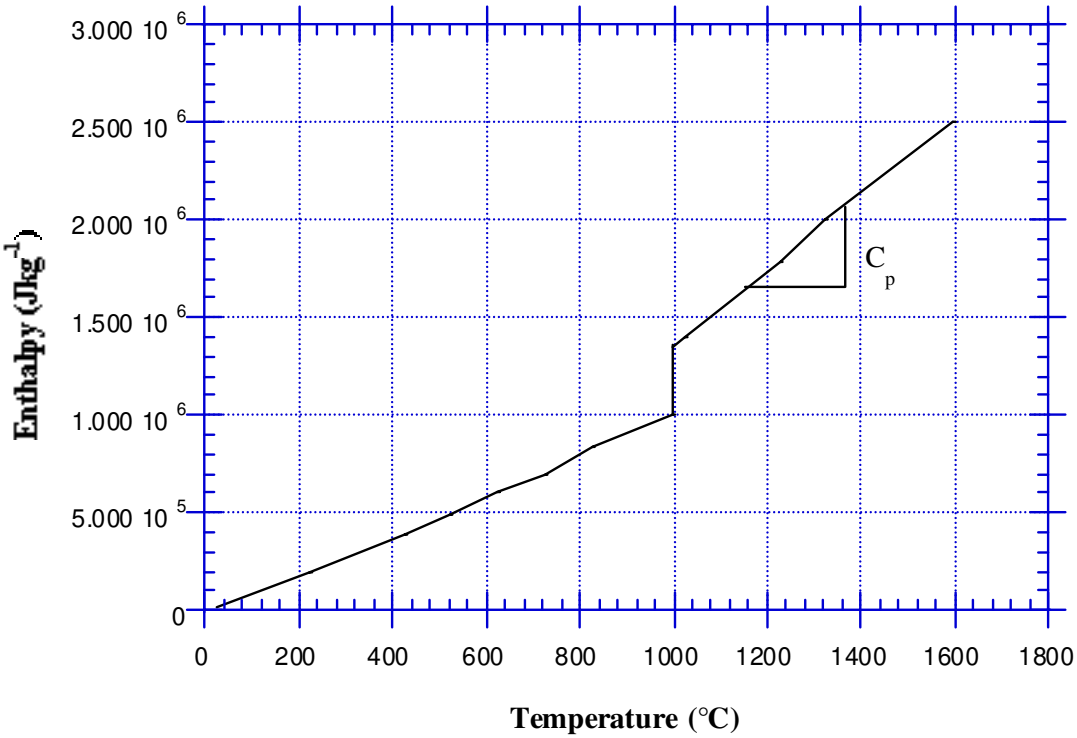

Figure 9: Enthalpy-temperature model for flux

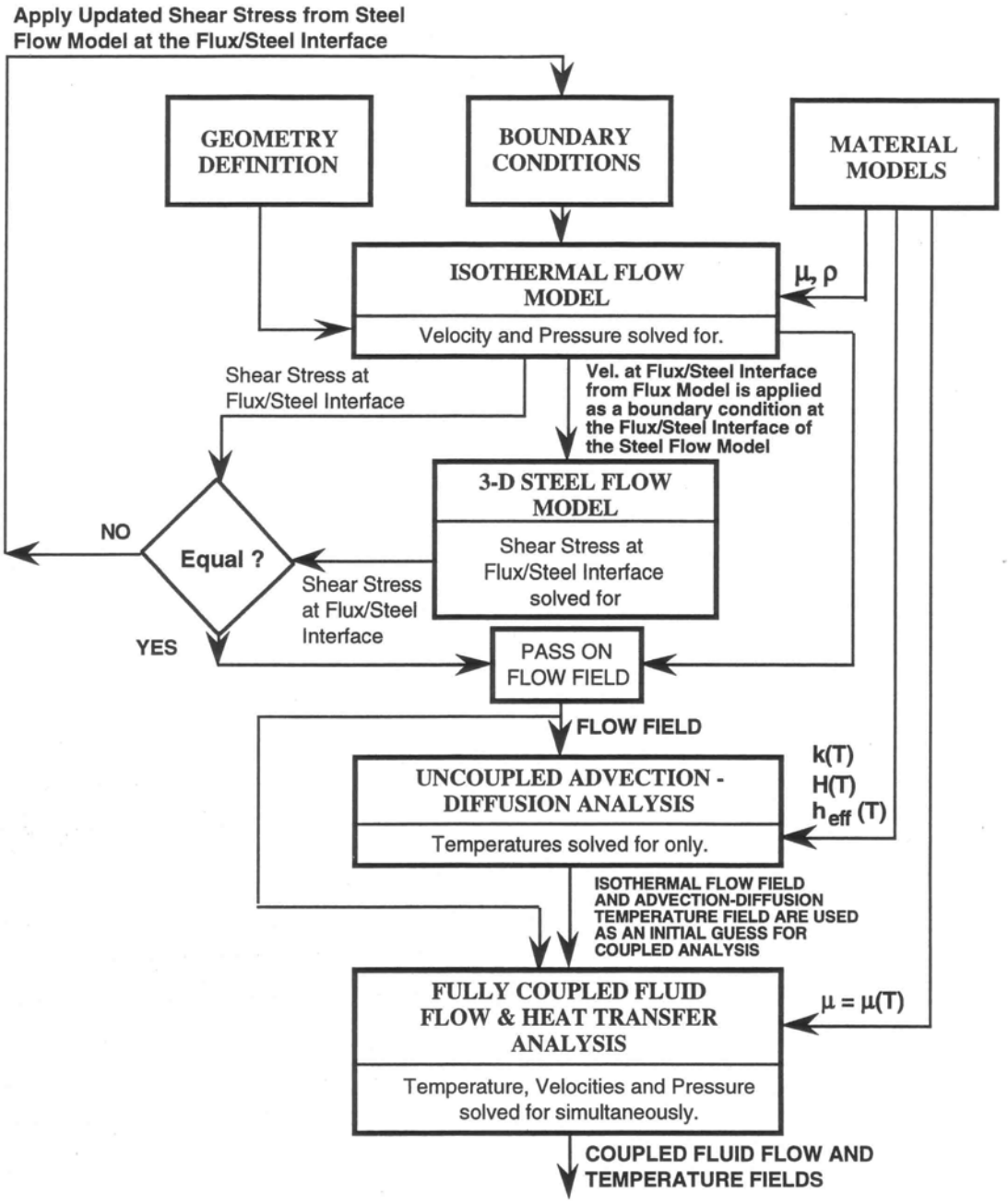

Figure 10: Flow chart of model solution methodology

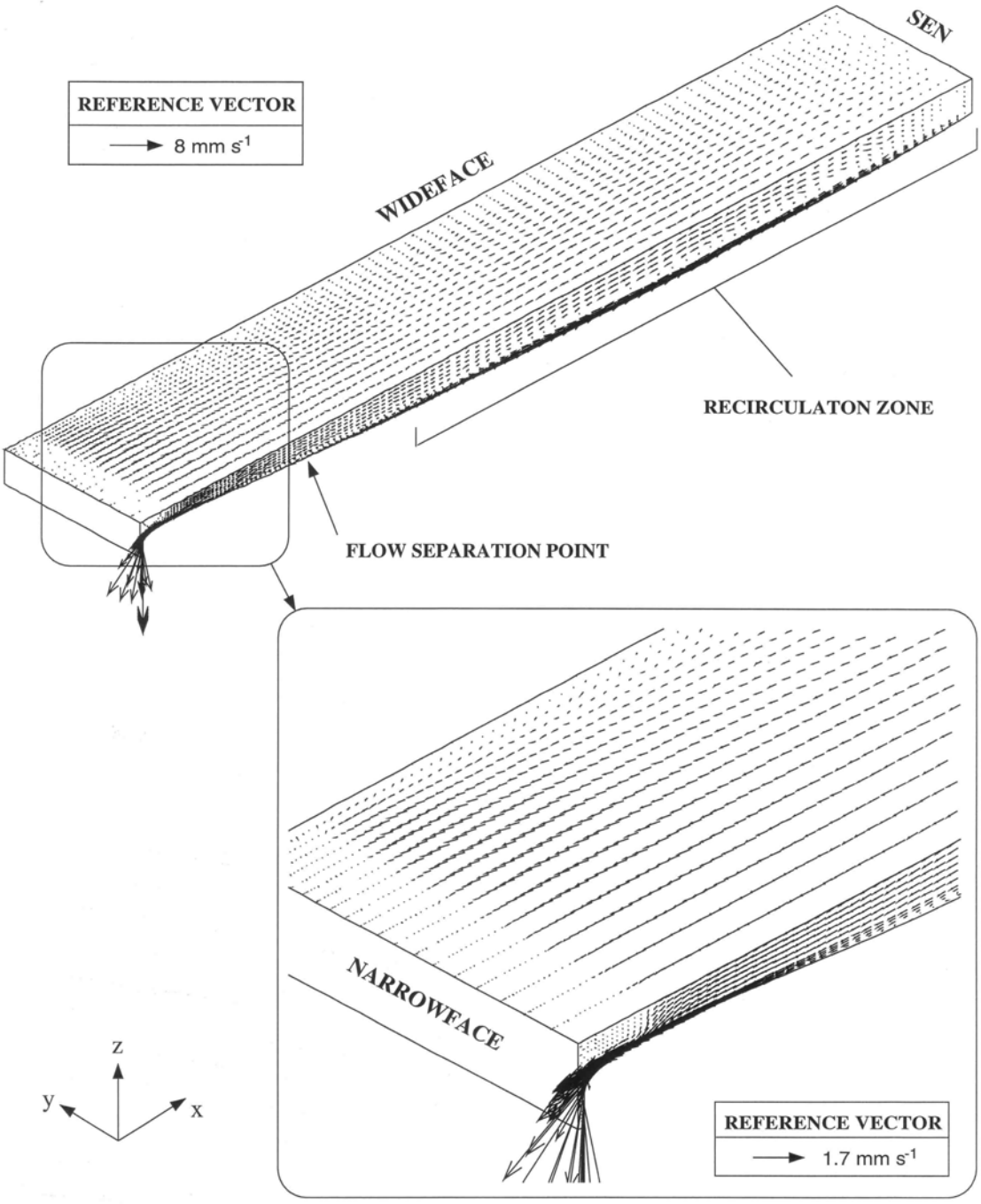

Figure 11: Calculated velocity distribution in flux layers at top surface and at mid-plane showing recirculation zone and flow separation (**standard conditions**)

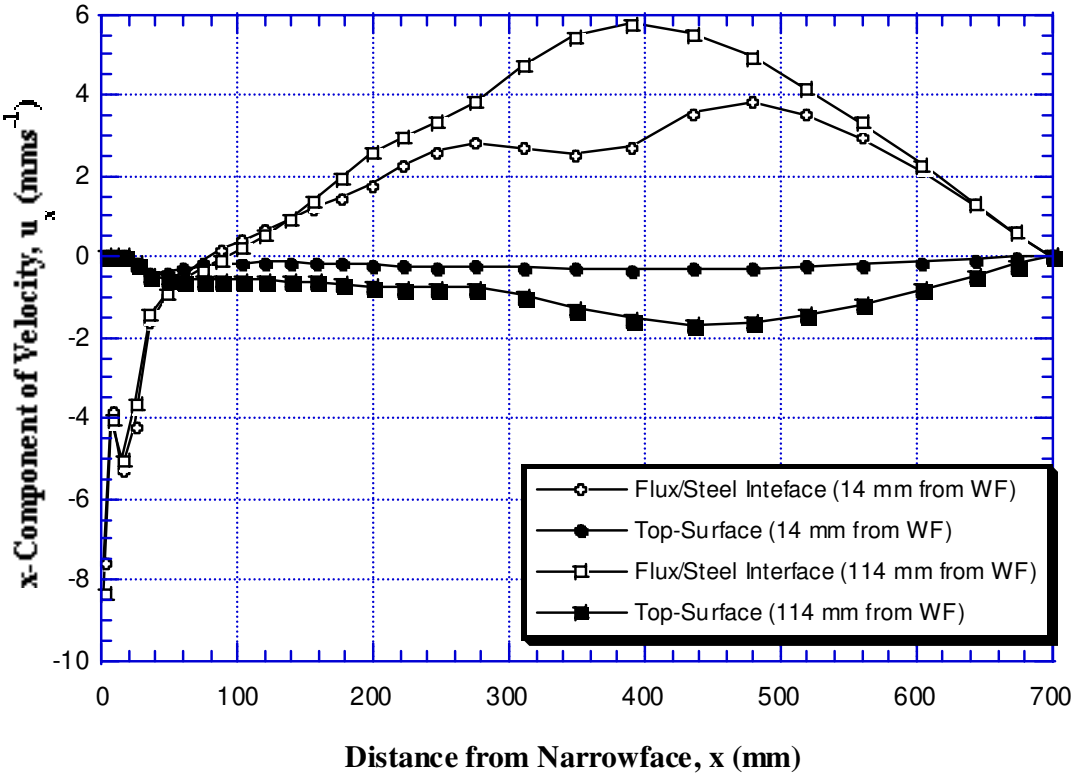

Figure 12: Top-surface and flux/steel interface velocity distribution as function of distance from narrowface

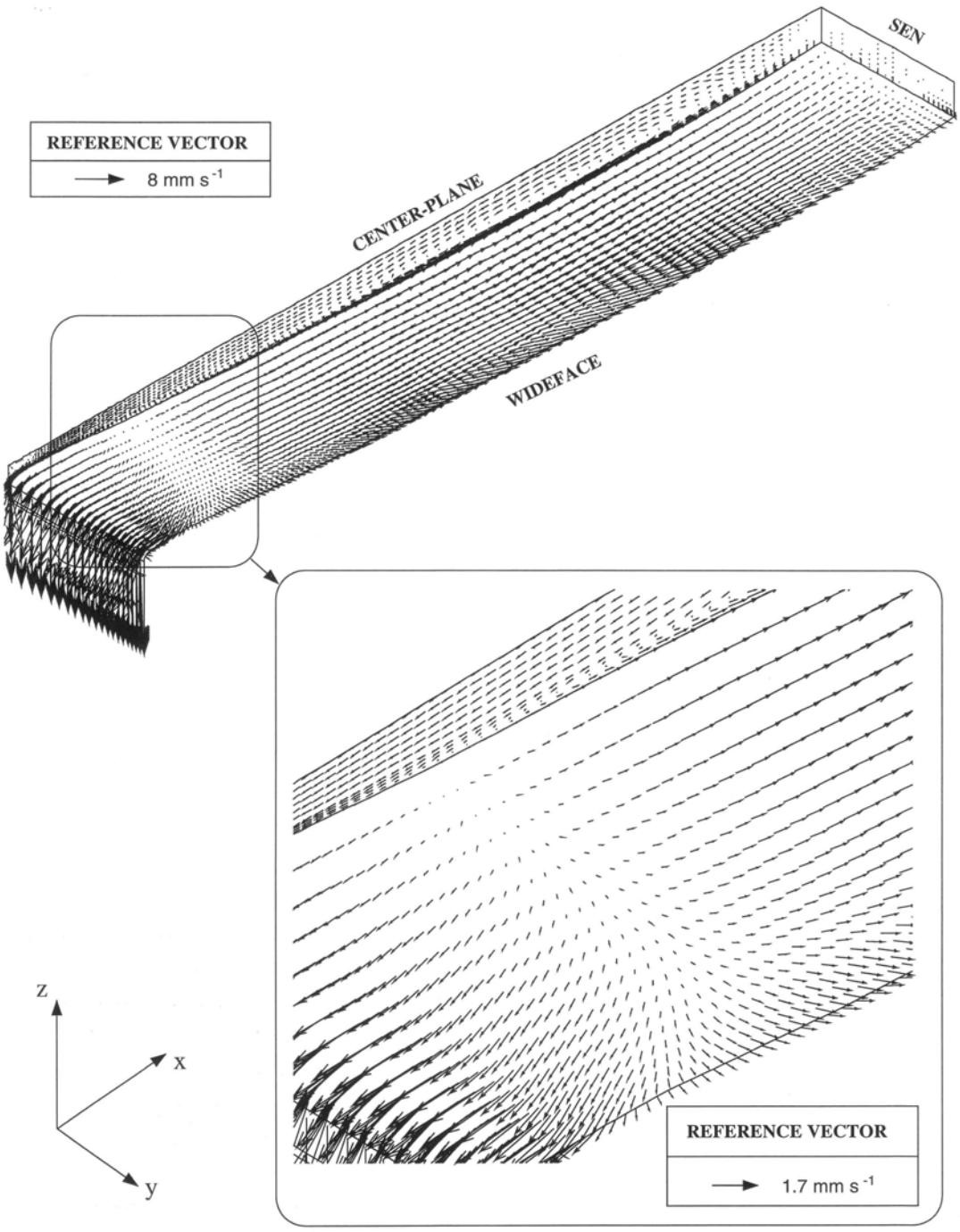

Figure 13: Calculated velocity distribution at flux/steel interface and at mid-plane showing flow separation and recirculation (**standard conditions**)

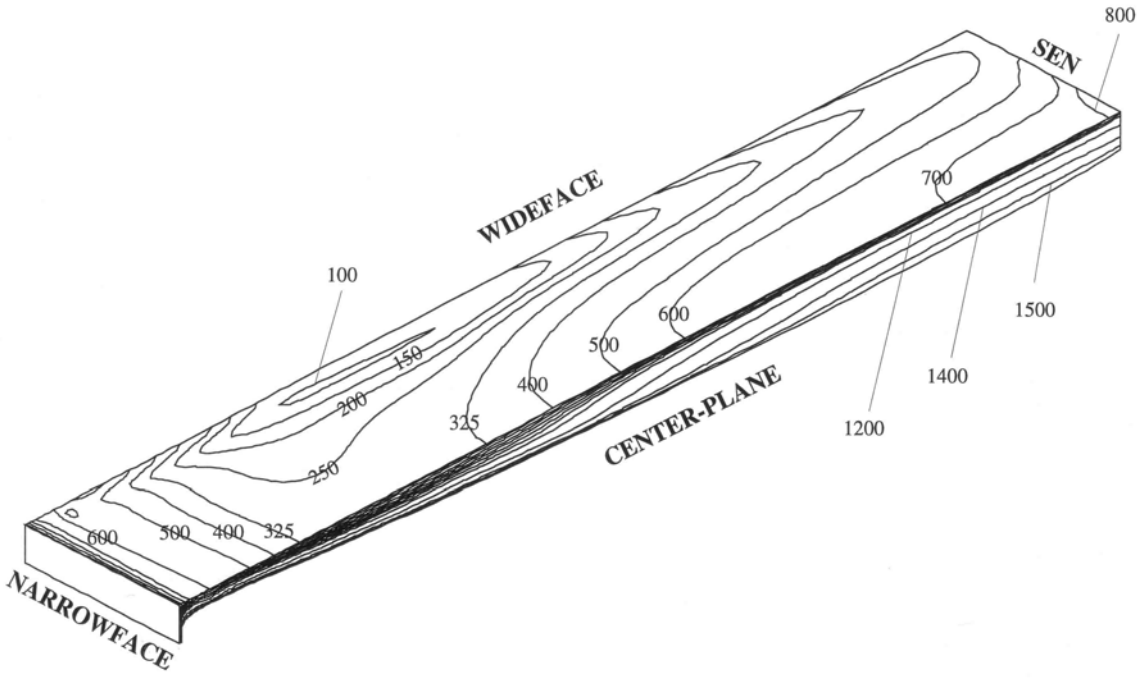

Figure 14: 3-D Temperature distribution calculated at flux surface and centerplane (°C, **standard conditions**)

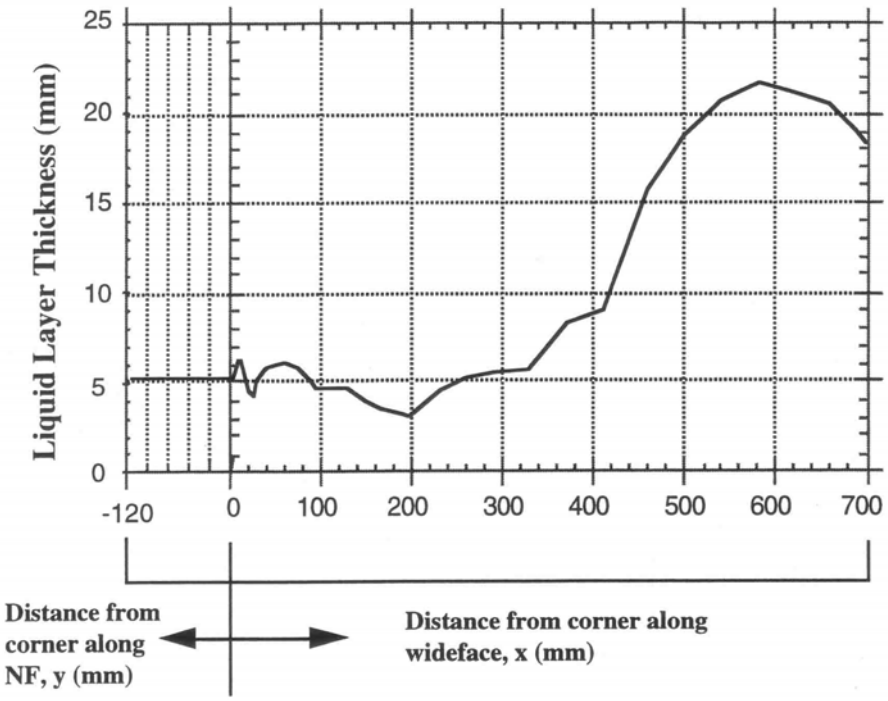

Figure 15: Liquid layer thickness around mold perimeter (**standard conditions**)

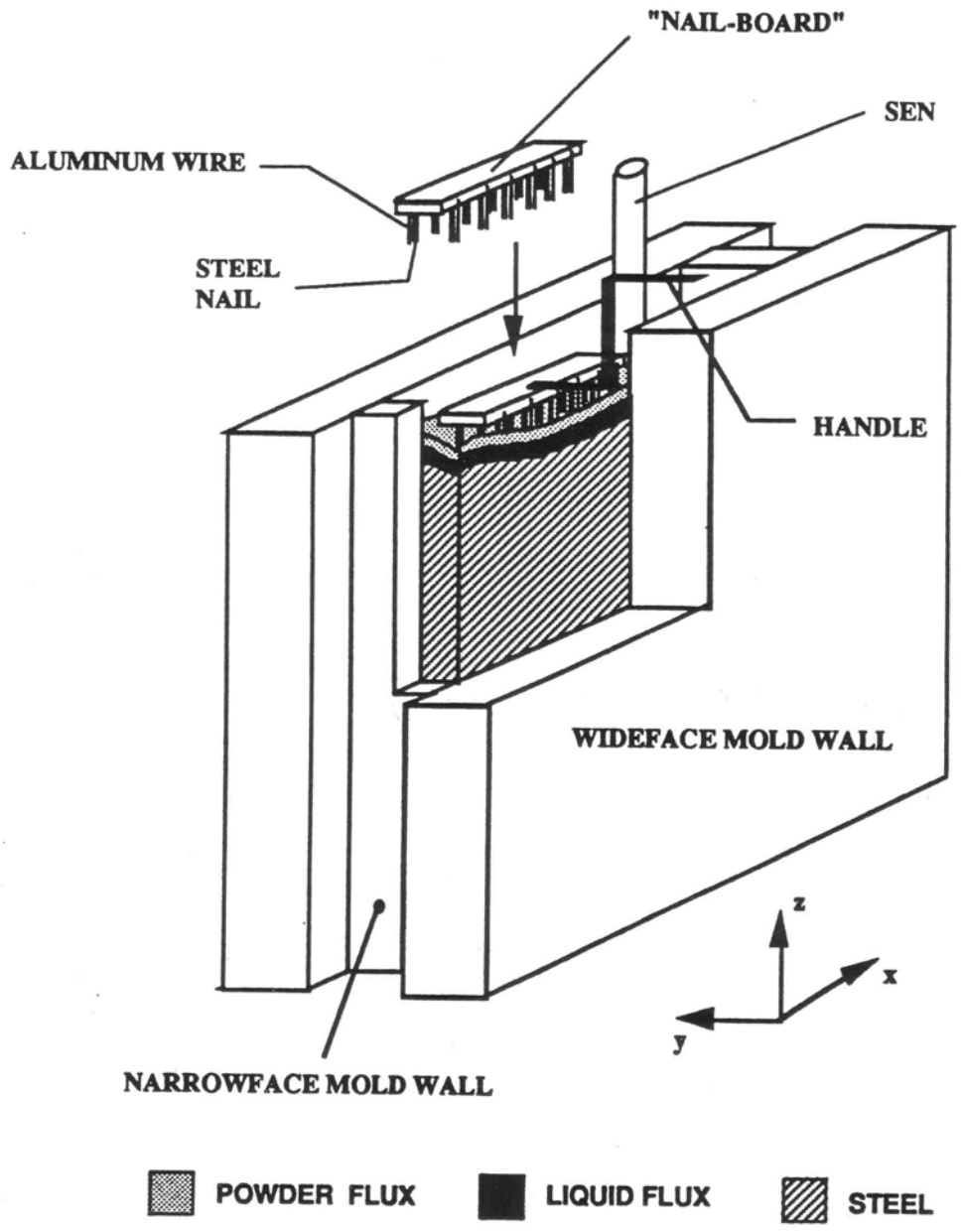

Figure 16: Schematic of layer thickness measurement method

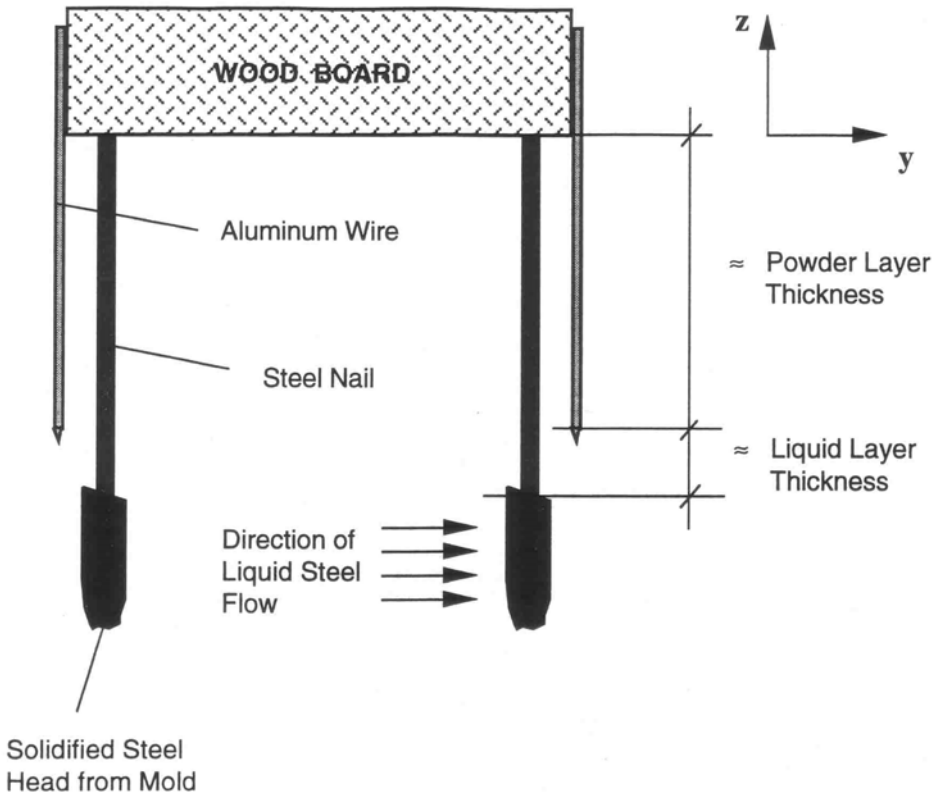

Figure 17: Close-up of cross-section through "nail-board"

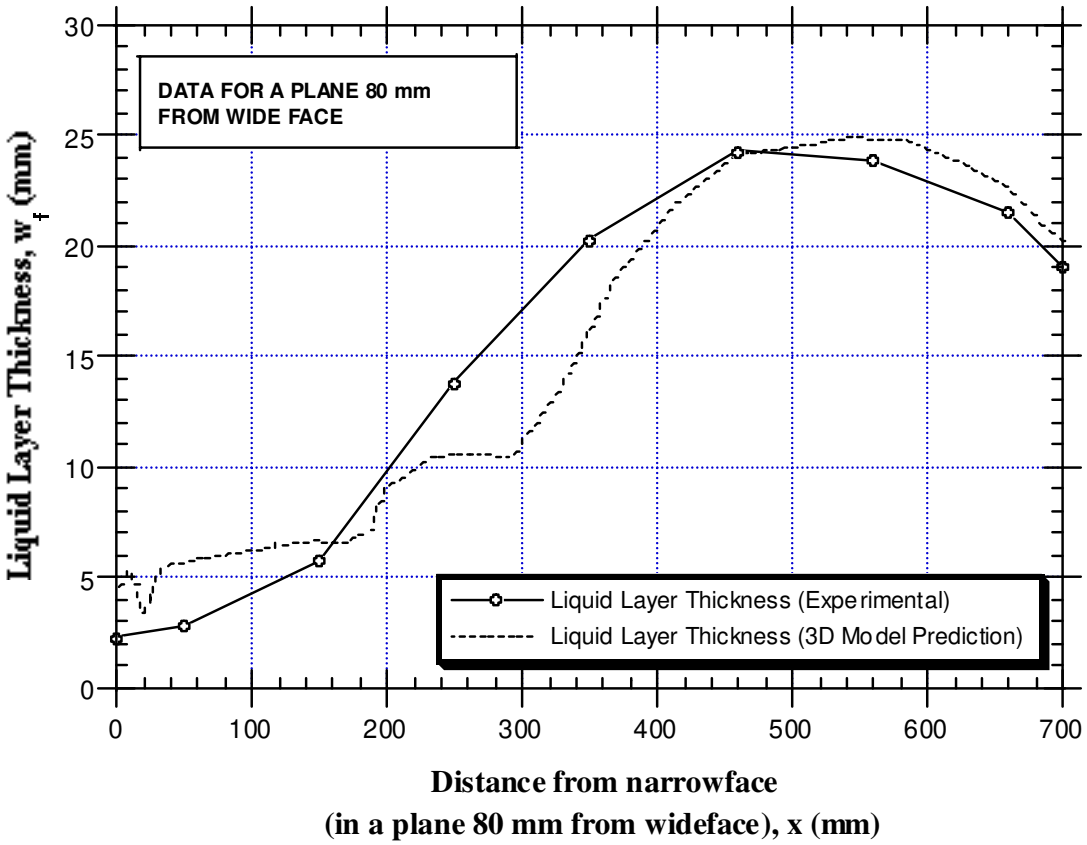

Figure 18: Comparison of measured and predicted liquid layer thickness

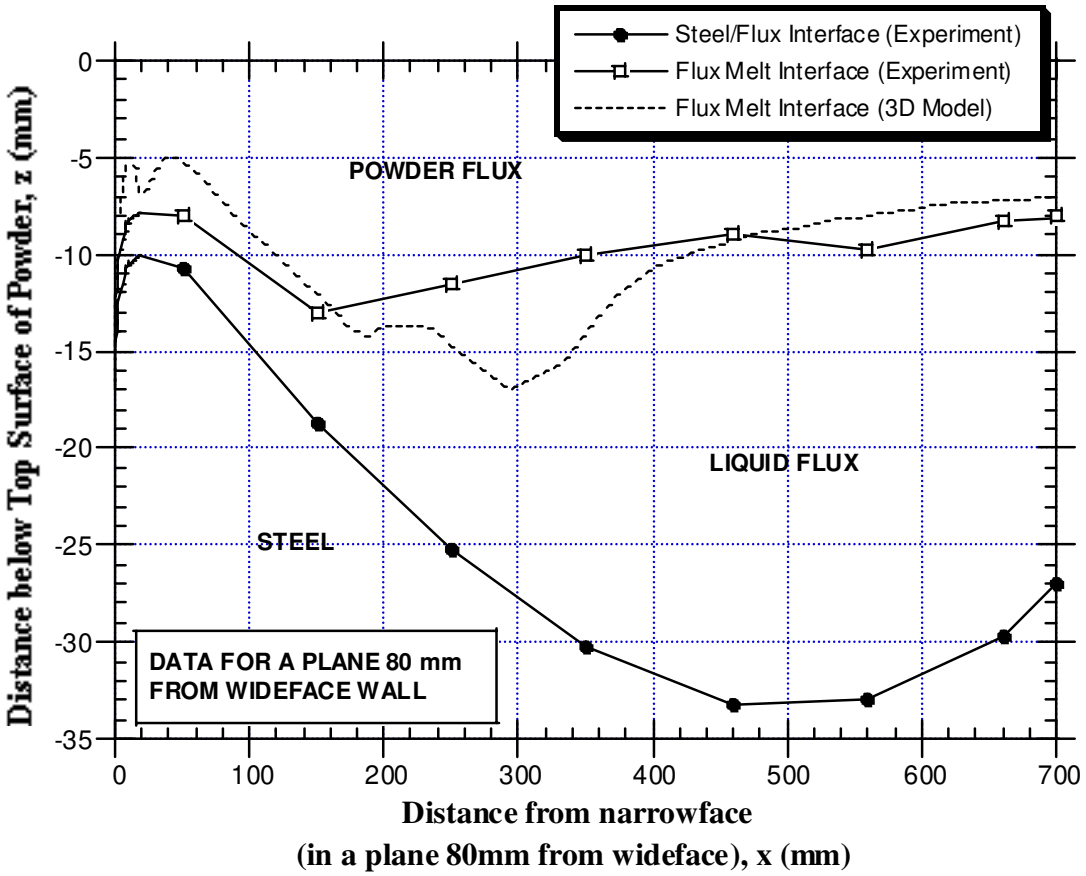

Figure 19: Comparison of measured and predicted melt-interface positions

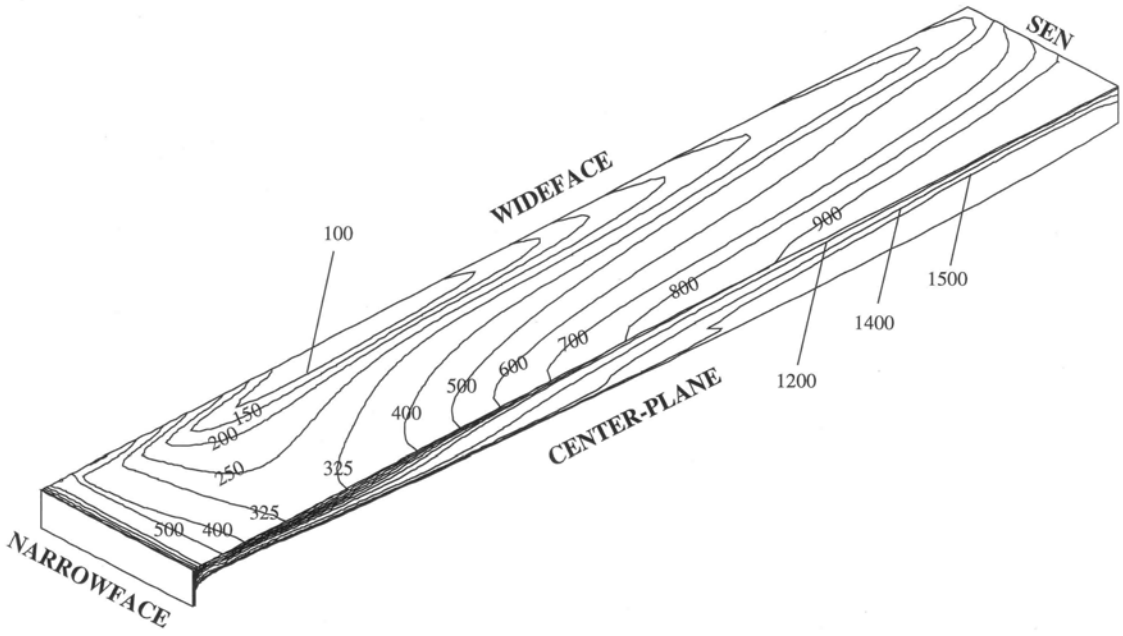

Figure 20: 3-D Temperature distribution calculated for flux with lower liquid viscosity. (temperatures in °C)

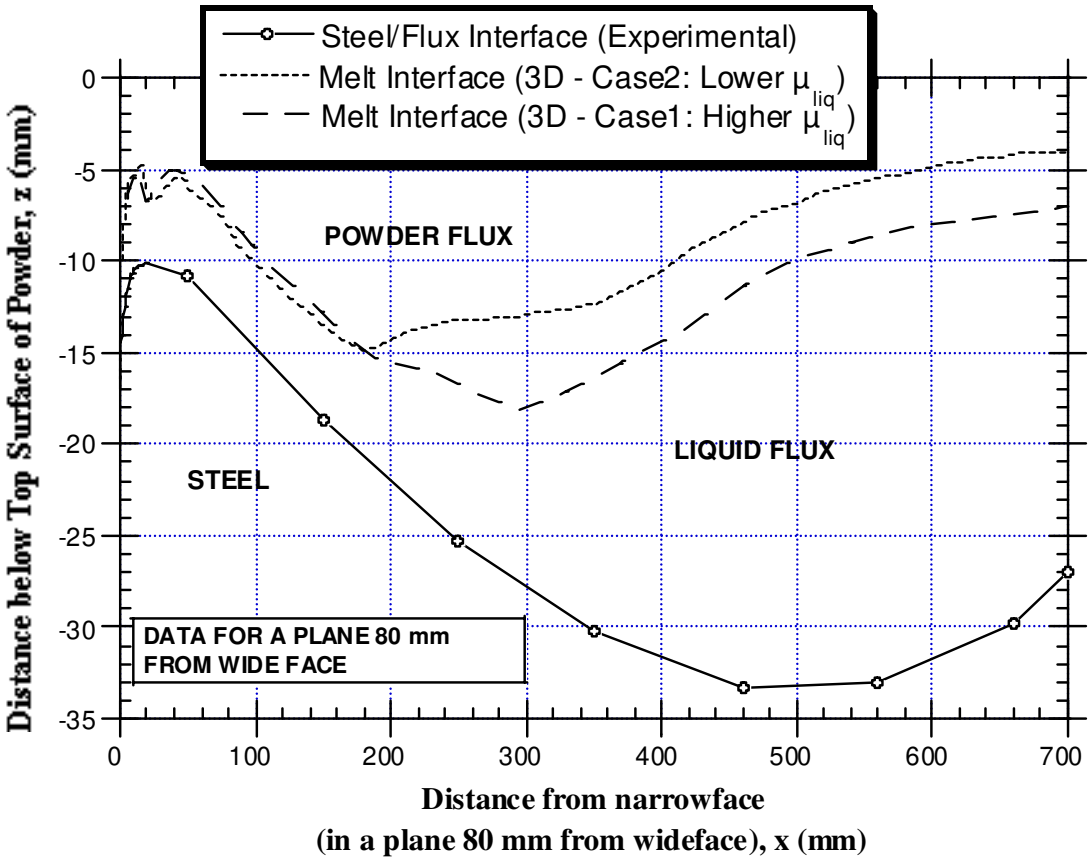

Figure 21: Effect of viscosity on average position of melt interface

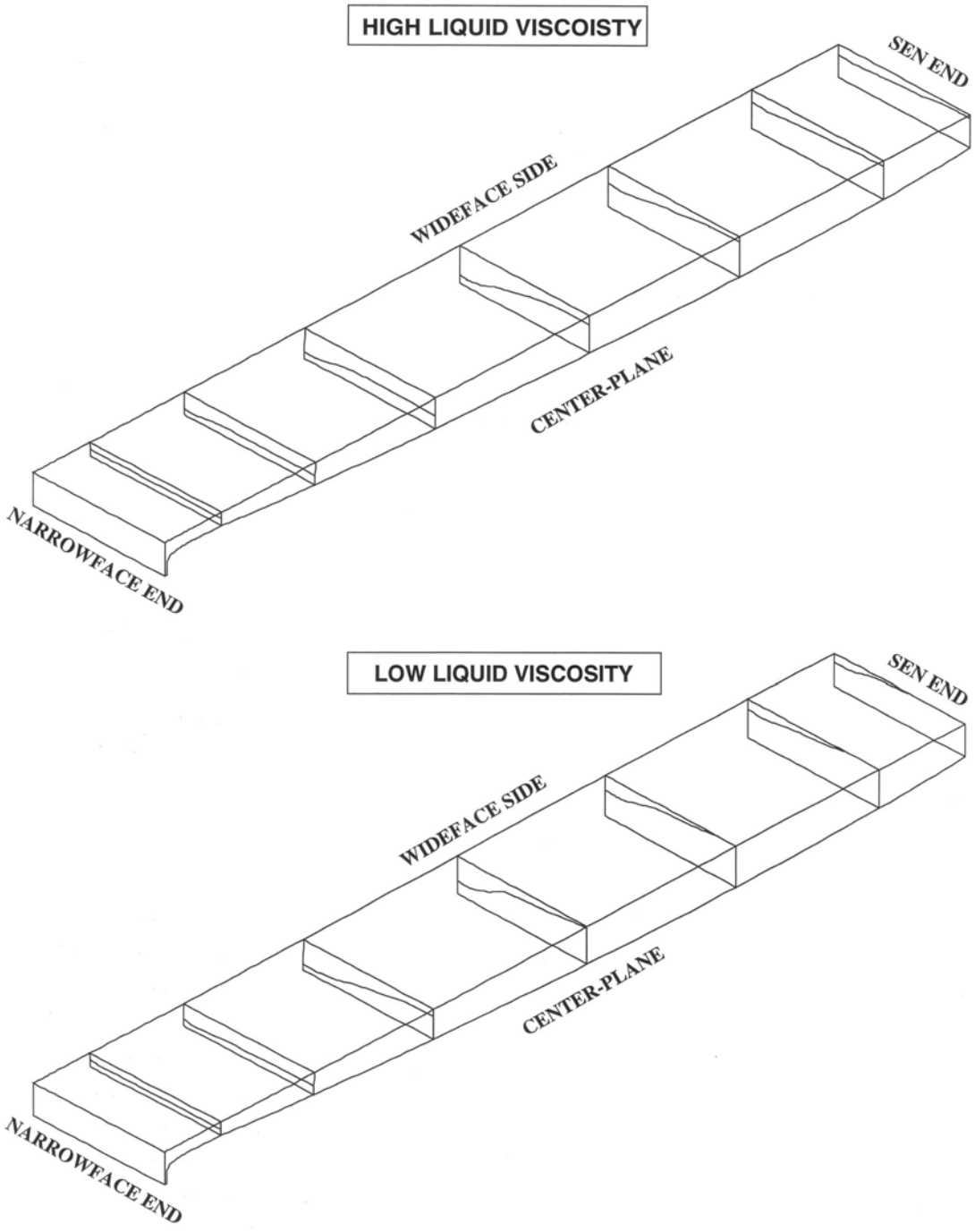

Figure 22: Positon of melt Interface at several locations in the mold as a function of liquid flux viscosity

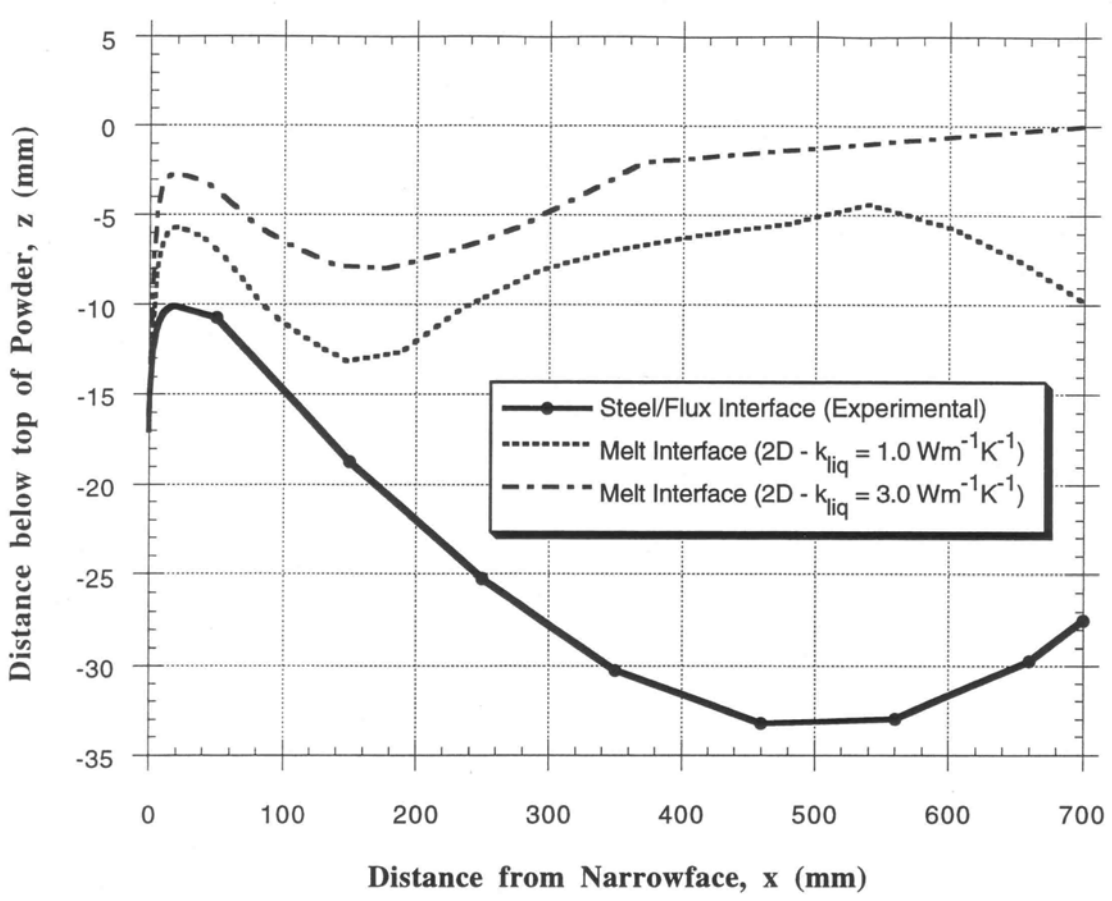

Figure 23: Effect of liquid thermal conductivity on location of melt interface

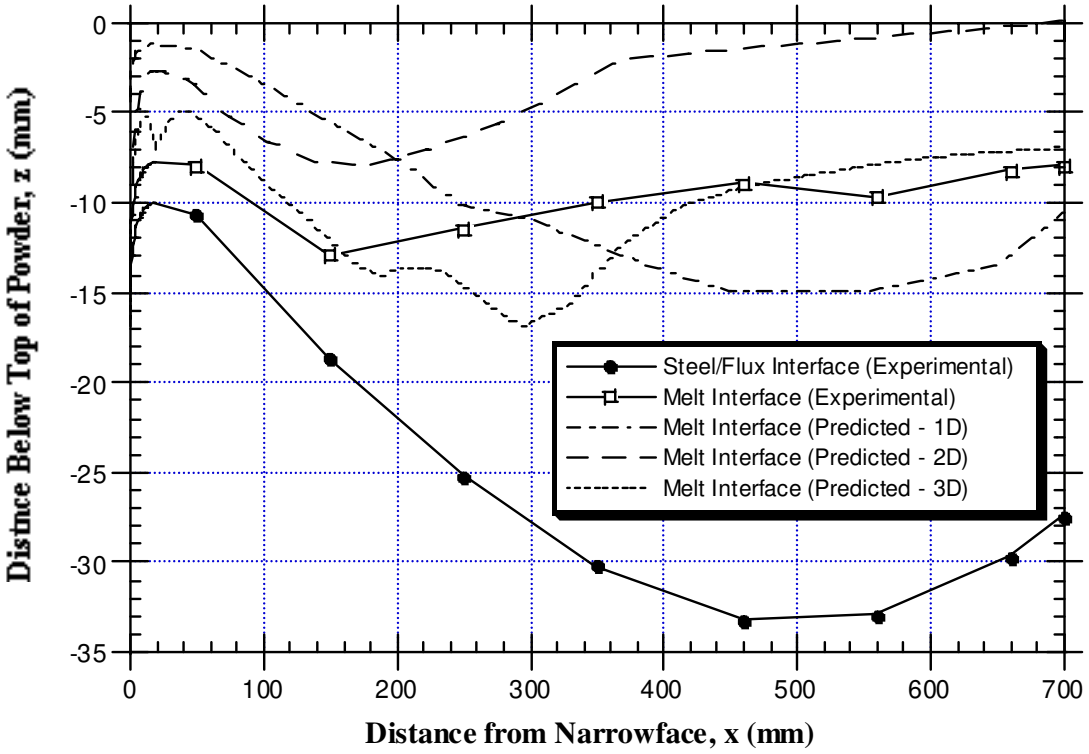

Figure 24: Comparison of prediction of melt interface location for 1-D, 2-D, and 3-D Models

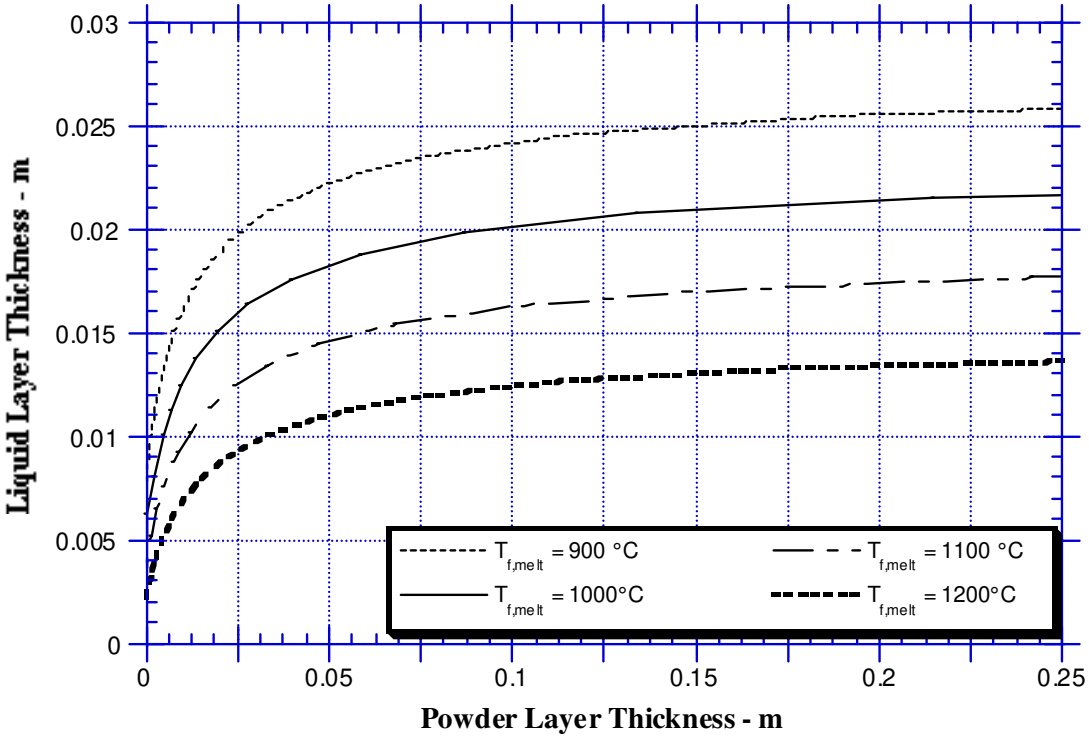

Figure 25: 1-D prediction of relationship between powder layer thickness and liquid layer thickness as a function of the flux melting temperature

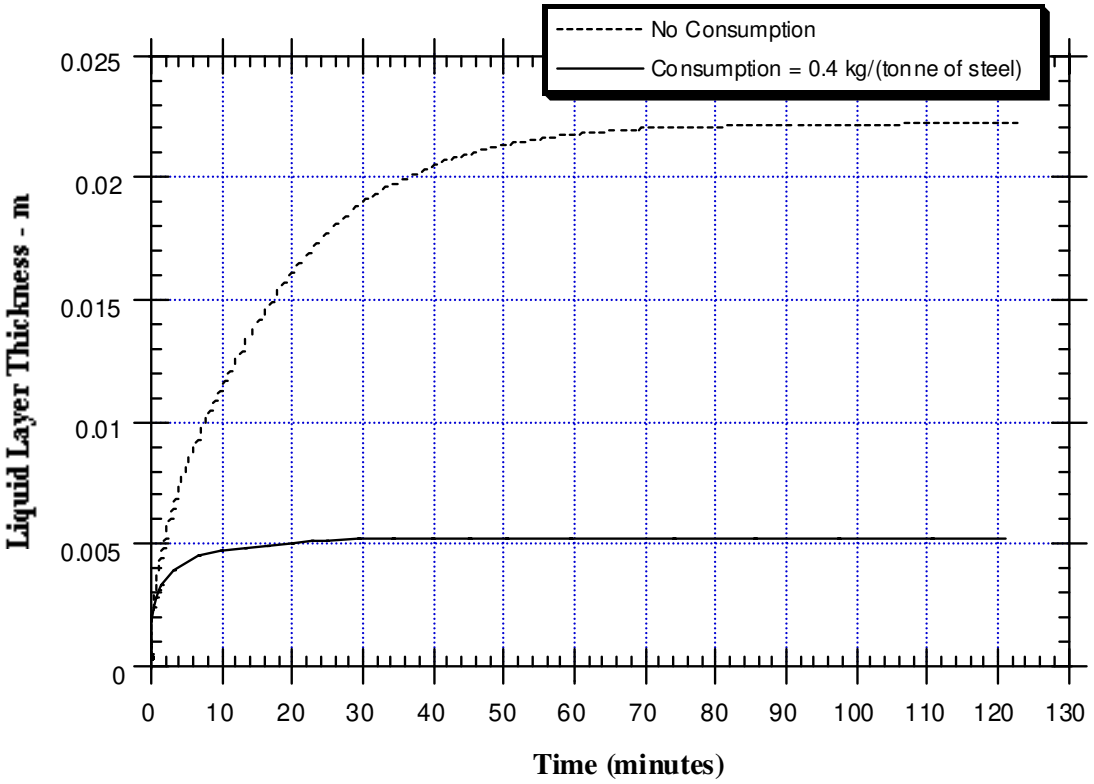

Figure 26: Effect of liquid flux consumption on time taken to achieve steady state

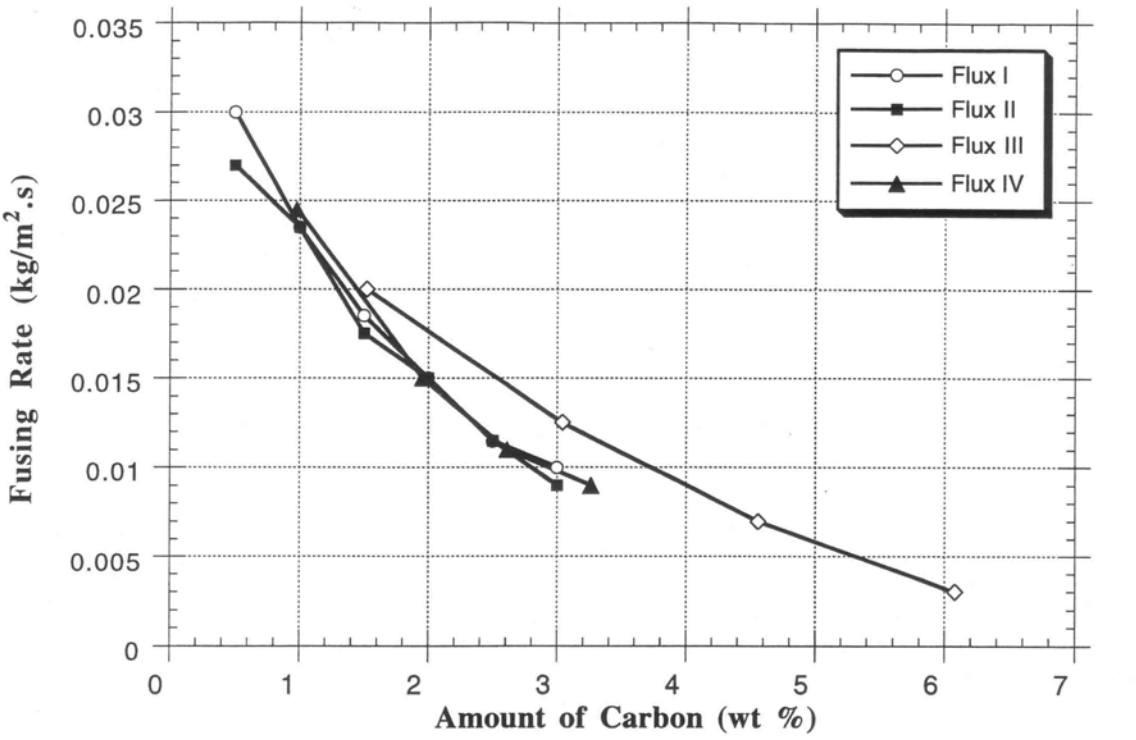

Figure 27: Effect of Carbon Content on Melting Rate of Flux[6]

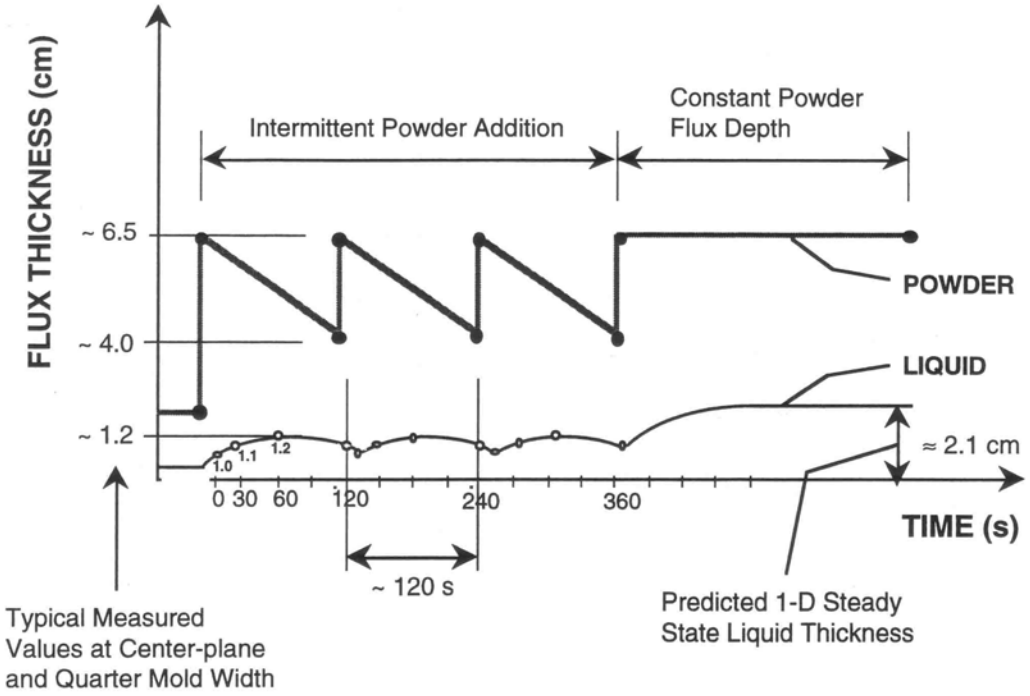

Figure 28: Transient schematic showing a possible effect of intermittent powder addtion. The points are typical measurements at the mold center-plane and quarter width[21].